ELSEVIER

Contents lists available at ScienceDirect

International Journal of Mechanical Sciences

journal homepage: www.elsevier.com/locate/ijmecsci





A hierarchical multiscale crystal plasticity model for refractory multi-principal element alloys

Weizheng Lu ^a, Yang Chen ^a, Wei Zhang ^b, Fusheng Tan ^a, Jia Li ^{a,*}, Bin Liu ^b, Peter K Liaw ^c, Qihong Fang ^{a,*}

- ^a State Key Laboratory of Advanced Design and Manufacturing for Vehicle Body, College of Mechanical and Vehicle Engineering, Hunan University, Changsha 410082, PR China
- ^b State Key Laboratory of Powder Metallurgy, Central South University, Changsha 410083, PR China
- ^c Department of Materials Science and Engineering, The University of Tennessee, Knoxville, TN 37996, USA

ARTICLEINFO

Keywords:

Refractory multi-principal element alloy Hierarchical multiscale framework Chemical short-range order Mechanical properties Strengthening mechanism

ABSTRACT

Refractory multiple principal elemental alloys (RMPEAs) show the excellent combinations of mechanical properties and oxidation resistance, are considered the most promising as the structural materials for aerospace industries and gas turbine. However, the quantitative contribution of microstructure on the strength and deformation mechanisms remains challenging at micrometer scale. In this work, we capture the lattice distortion and chemical short-range order (CSRO) using atomic simulation, and introduce them into the hierarchical multiscale model to study the strengthening mechanism and plastic behavior in the body-centered cubic HfNbTa RMPEA. The results show that the ultrastrong local stress fluctuation greatly improves the dislocation-based strength, causing the significant dislocation forest strengthening in the annealed state. The dislocation slip would be suppressed for raising the strength and increasing the difficulty of the plastic deformation in the annealed HfNbTa. Thus, the existence of the CSRO structure effectively enhances the strength, in a good agreement with the experiment. The inhomogeneous degree of the stress distribution become more serious at the high strain, responding well to the plastic deformation of the high-strength HfNbTa. Moreover, the Ta-rich locally ordered structure leads to an obvious heterogeneous strain and stress partitioning, which forms a strong strain gradient in the adjacent grain interiors and contributes to the strong back-stress-induced strain hardening in the annealed HfNbTa. Our findings give an insight into exploring MPEAs with desired mechanical properties via tailoring CSRO by utilizing thermomechanical processing.

1. Introduction

The multi-principal element alloys (MPEAs) with the complex concentrated solutions composed of multiple principal elements have attracted much attention due to their excellent properties [1–6]. The random distributions of the atoms with different types and sizes in the lattice produce the severe atomic-scale lattice distortion, and thus result in the good mechanical properties, such as high ductility and strength [1–3], good fatigue resistance [4], remarkable corrosion resistance [5], and high impact resistance [6]. In recent years, some MPEAs containing refractory elements (including Nb, Zr, Hf, W, Ti, V, Cr, Mo and Ta) have garnered a significant amount of interest due to the extremely high melting point and excellent softening resistance. Refractory multi-principal element alloys (RMPEAs) are considered as ideal

candidates for high temperature applications [3,7]. Their yield strengths are much higher than that of nickel-based superalloys at high temperature [8], which meet the strong demand of the next generation of nuclear reactors and jet engines for increasing the operating temperature.

However, the near ideal chemical random state is only possible at high temperatures. At ambient temperature, the complex enthalpy interaction between different constituent elements leads to the preference (or avoidance) of atomic bonding, which forms different degrees of chemical short-range order (CSRO) to reduce the free energy of the system [3,9]. The lattice distortion field is strongly dependent on the degree and distribution of local element enrichment region, which affects the dislocation nucleation/movement, strain hardening and macroscopic properties [2,9,10]. It is expected that the CSRO structure is highly adjusted through the processing condition to design the MPEAs

E-mail addresses: lijia123@hnu.edu.cn (J. Li), fangqh1327@hnu.edu.cn (Q. Fang).

^{*} Corresponding authors.

with the targeted mechanical properties [3]. Recently, many experiments and simulations have explored the influence of locally ordered structure on the mechanical properties of MPEA. The direct observation of CoCrNi MPEA by transmission electron microscope shows that the increase of CSRO leads to higher stacking fault energy and hardness [11]. Density functional theory calculations show that the presence of CSRO structure not only narrows the dislocation core energy distribution and reduces the spatial heterogeneity of dislocation core energy in MoNbTaW RMPEA [12], but also affects the phase energy and stacking fault energy in CrCoNi MPEA [3]. The atomic simulation results show that CSRO improves the activation barrier for govern dislocation activity, and enhances the robustness of the energy landscape [13,14]. Moreover, the locally ordered structure affects the selection of dislocation pathways, and increases the lattice friction on dislocation motion through the nanoscale segment detrapping mechanism [13,14]. However, the relationship between locally ordered degree and mechanical properties in the MPEA is still unclear due to its extreme difficulty to control locally ordered structure using experiments [15].

The influence of CSRO on mechanical behavior of materials is multiscale, including atomic scale lattice distortion, micrometer scale dislocation movement, macroscale strain hardening, and macroscale mechanical response. To study the influence of the existence of locally ordered structure at the nanoscale on the strength contribution and macroscale deformation behavior, it is an optional breakthrough to analyze the cross-scale microstructure synergetic deformation mechanism at the considerable length scales [16]. Although molecular dynamics (MD) simulation accurately captures the mobility and atomic-scale strain information of a single dislocation in the lattice distortion field [10,17], it requires high computational costs for the large-scale systems. Therefore, a simulated method with the effective time and cost need investigates the large-scale deformation behavior of RMPEA. The multi-scale method is one of the computing technologies that use multiple models of different scales to describe the mechanical behavior of materials. It provides an effective approach to establish the constitutive law of the problem from the first principle or even from more basic scientific basis. The existing multi-scale strategies are divided into two categories: "concurrent" and "sequential" methods [18]. In the concurrent multi-scale method, the analysis is performed simultaneously at different scales. The sequential multiscale method provides the required parameters for the large-scale model through small-scale analysis as the pretreatment of the large-scale model [19], which uses the homogenization and averaging method on the corresponding representative volume element (RVE) to define the kinematic parameters and stress tensors at each material point of the large-scale RVE. A non-Schmid crystal plastic constitutive model on two length scale is presented to study the thermodynamic behavior of nickel-based superalloys in a wide temperature range from 300 K to 1223 K [20]. A temperature-dependent hierarchical multiscale method by introducing Cauchy-Born boundary is developed to simulate the edge and surface effects in nanoscale metal materials [21]. A continuous-atomic multiscale program based on hierarchical RVE is proposed to simulate the nonlinear behavior of nanoscale materials [22]. A hierarchical thermodynamic multi-scale technology is proposed to study the thermodynamic behavior of nanocrystalline alloy in the presence of edge dislocation by transferring the mechanical properties of atomic RVE to the finite element node [23]. The multi-scale model of FCC MPEAs established could effectively capture the inhomogeneous strain field dominated by lattice distortion, and the accuracy is verified by comparison with the experiment [24].

In this work, a generalized hierarchical multiscale crystal plasticity framework (Fig. 1) is proposed to investigate the effect of microstructures on body centered cubic (BCC) RMPEAs at different scales (nanoscale, microscale, and mesoscale). The lattice strain fluctuations dominated by locally ordered structure are captured successfully, and the effects of CSRO on the strengthening mechanism and plastic behavior of BCC HfNbTa RMPEA are studied. At the nano- and micro-

scales, based on the MD/MC simulation and experiment, the heterogeneous lattice strain field caused by CSRO is transferred to the discrete dislocation dynamics (DDD) simulation to study the influence of the chemical concentration fluctuations on the dislocation motion mode. At the meso-scale, the material information with the interaction between dislocations and inhomogeneous strain field are imported into the crystal plastic finite element (CPFE) simulations. The accuracy and rationality of the simulation results are verified by comparing the predicted stress-strain response with the experimental observations in the HfNbTa RMPEA [25], and the plastic deformation behaviors at meso-scale are analyzed in as-cast and annealed polycrystalline HfNbTa RMPEAs.

Here, the organization of this paper is the following. Section 2 presents the CP constitutive model, the coupling strategy from various length scales, and the material parameters transmitted between different scales. In Section 3, the basic setup of the multiscale framework including the nanoscale MD/MC simulation, microscale DDD simulation, and mesoscale CPFE simulation is described. Section 4 show the computation of hierarchical multiscale crystal plasticity model. Section 5 summarizes the results and discussions for deformation and strengthening of HfNbTa RMPEA.

2. Multiscale framework

In this section, the crystal plasticity constitutive model used in this work has been reviewed. Next, the coupling strategy of hierarchical multiscale models has been developed to transfer the material parameters between simulation tools of different scales.

2.1. Review of crystal plasticity model

To capture the plastic deformation behaviors of HfNbTa RMPEA at the meso-scale, the constitutive behavior of polycrystalline materials is illustrated by a rate-dependent crystal plastic model [26]. In the continuous theory, the total deformation gradient tensor maps the infinitesimal points in the reference configuration to the corresponding points in the deformed configuration. The total deformation gradient tensor is decomposed into the elastic and plastic components [27]:

$$\mathbf{F} = \mathbf{F}^{\mathbf{c}} \mathbf{F}^{\mathbf{p}} \tag{1}$$

where F^e is the elastic deformation gradient to describe the rigid rotation and stretch of lattice, and F^p is the plastic deformation gradient to represent the nonlinear plastic deformation.

The velocity gradient is decomposed into the elastic and plastic components:

$$\mathbf{L} = \dot{\mathbf{F}}\mathbf{F}^{-1} = \dot{\mathbf{F}}^{e}\mathbf{F}^{e-1} + \mathbf{F}^{e}\dot{\mathbf{F}}^{p}\mathbf{F}^{p-1}\mathbf{F}^{e-1}$$
(2)

The plastic component of the velocity gradient on the intermediate structure is expressed as lattice shear along the specific crystal slip direction on different crystal slip planes:

$$\mathbf{L}^{p} = \dot{\mathbf{F}}^{p} \mathbf{F}^{p-1} = \sum_{\alpha=1}^{N_{slip}} \dot{\gamma}^{\alpha} \mathbf{P}^{\alpha}, \mathbf{P}^{\alpha} = \mathbf{m}_{0}^{\alpha} \otimes \mathbf{n}_{0}^{\alpha}$$
(3)

where \mathbf{P}^{α} is the Schmid orientation tensor defined by the slip direction vector \mathbf{m}_{0}^{α} and the slip plane vector \mathbf{n}_{0}^{α} of the α^{th} slip system. $\dot{\gamma}^{\alpha}$ is the plastic strain rate, determined by the resolved shear stress and slip system deformation resistance:

$$\dot{\gamma}^{a} = \dot{\gamma}_{0} \left| \frac{\tau^{a} - \tau_{b}}{\tau_{sr}^{a}} \right|^{1/m} sign(\tau^{a} - \tau_{b})$$
(4)

where $\dot{\gamma}_0$ is the reference plastic strain rate to describe the macroscopic plastic strain rate, τ^{α} is the resolved shear stress (RSS), τ_b is the kinematic hardening effect caused by the back stress, τ^{α}_{sr} is the slip system

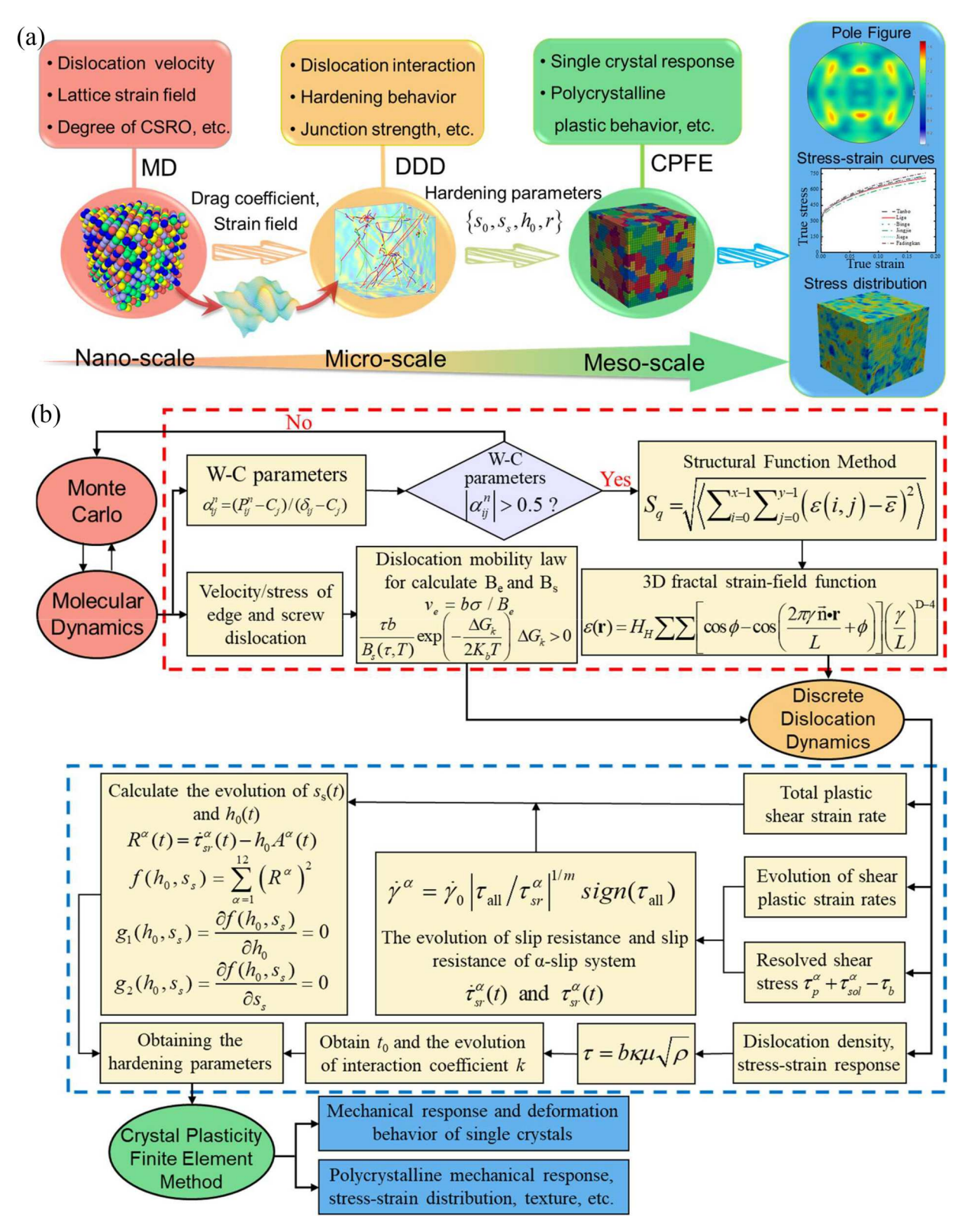


Fig. 1. (a) Schematic diagram of hierarchical multiscale crystal plasticity strategy. **(b)** The flowchart for parameter calibration procedure of hierarchical multiscale crystal plasticity framework. The computed methods of the atomic-scale, micron-scale, and meso-scale are described as different colors in Fig. (a), and the calculation process of the corresponding scale is presented by the same color in Fig. (b). From Fig. (b), the multi-scale calculation process includes the five parts: (i) Dislocation velocity and CSRO parameter are simulated through MD/MC simulations; (ii) The mobility of screw and edge dislocations and the atomic-scale heterogeneous strain field induced by local ordered structure are calculated, and then introduced into DDD simulation; (iii) Seven single crystals of RMPEA are established to simulate the mechanical behavior through DDD simulations; (iv) By coupling the DDD simulations with CP constitutive model, the hardening parameters of single crystal required for CPFE simulations are calculated. The mechanical response of the single crystal is obtained through CPFE simulation; (v) The hardening parameters of single crystals are calculated to obtain the hardening parameters for the polycrystalline RVE, and then get the stress-strain curve, texture, and stress distribution.

deformation resistance, m is the sensitivity exponent, and sign is the signum function.

The RSS for the driving force of dislocation movement is expressed as:

$$\tau^{\alpha} = (\mathbf{F}^{\mathrm{eT}} \mathbf{F}^{\mathrm{e}} \mathbf{S}) : \mathbf{P}^{\alpha}$$
 (5)

which S represents the second of Piola-Kirchhoff stress. When τ^{α} reaches the corresponding critical value, the α -slip system is activated. The critical value is related to the resistance to overcome the process of dislocation movement.

The relationship between the second Piola-Kirchhoff stress tensor and the Green-Lagrange strain tensor \mathbf{E}^e is given by the generalized Hooke's law:

$$\mathbf{S} = \mathbb{C} : \mathbf{E}^{\mathbf{e}} \tag{6}$$

where $\mathbb C$ is the fourth-order anisotropic elasticity tensor. For the BCC lattice, the matrix of $\mathbb C$ depends on the elastic constants of C_{11} , C_{12} and C_{44} .

The Green-Lagrange strain tensor is expressed as:

$$\mathbf{E}^{\mathbf{e}} = \frac{1}{2} \left[\mathbf{F}^{\mathbf{e}\mathsf{T}} \mathbf{F}^{\mathbf{e}} - \mathbf{I} \right] = \frac{1}{2} \left(\mathbf{F}^{\mathbf{p}-\mathsf{T}} \mathbf{F}^{\mathsf{T}} \mathbf{F} \mathbf{F}^{\mathbf{p}-1} - \mathbf{I} \right)$$
(7)

where I denotes the second-order identify tensor.

The evolution of back stress, τ_b , is modeled using a two-term Ohno-Wang type evolution law [28]. The definitions of two independent back stress components of α -slip system, i.e., χ_1^{α} and χ_2^{α} , are as follows

$$\dot{\chi}_{i}^{\alpha} = h_{i}\dot{\gamma}^{\alpha} - r_{i} \left(\frac{\left|\chi_{i}^{\alpha}\right|}{b_{i}}\right)^{m_{i}} \chi_{i}^{\alpha}\dot{\gamma}^{\alpha}; (i=1,2)$$

$$\dot{\chi}^{\alpha} = \sum_{i=1}^{2} \dot{\chi}_{i}^{\alpha}, \chi_{i}^{\alpha}(t=0) = 0; (i=1,2)$$
(8)

where r_i and h_i are the material parameters, and b_i = h_i/r_i . The exponent m_i governs the dynamic recovery of materials, which becomes more dominant when the stress approaches saturation value. Above equation approaches a piecewise linear function when m_i is large, while for m_i = 0, Eq. (8) reduces to the Armstrong-Frederick equation.

The slip system deformation resistance on α -slip system evolves according to the following equation [29]:

$$\dot{\tau}_{sr}^{\alpha} = \sum_{\beta} h^{\alpha\beta} |\dot{r}^{\beta}| \tag{9}$$

and

$$h^{\alpha\beta} = \left[q_0 + (1 - q_0) \delta^{\alpha\beta} \right] h^{\beta} \tag{10}$$

where q_0 is the latent hardening coefficient, and $\delta^{\alpha\beta}$ is the Kronecker delta. The latent-hardening parameter h^{β} is defined using a power-law relationship:

$$h^{\beta} = h_0^{\beta} \left[1 - \frac{\tau_{sr}^{\beta}}{S_r^{\beta}} \right]^{r^{\beta}} \tag{11}$$

where h_0^{β} is the initial hardening parameter of β -slip system, r^{β} is the sensitivity exponent between slip resistance and hardening moduli in β -slip system, and s_s^{β} determines the maximum slip resistance of any slip systems. The slip may occur on 48 different slip systems in BCC material, and these slip systems represent three different planes: 12 in the {112} family, 12 in the {110} family, and 24 in the {123} family. Approximate material behavior is calculated by considering a subset of total slip systems. In this manner, 12 slip systems of {110} family are considered based on the previous study [26]. According to the previous work [26, 30], the input parameters of $\{s_0, s_s, h_0, r\}$ have the same value of all slip systems for CPFE simulations.

2.2. Multiscale coupling strategy

To study the CSRO effect on the plastic deformation, a hierarchical multiscale crystal plasticity model is developed, and the flowchart of parameter calibration is presented in Fig. 1. Here, each scale is described as different colors in Fig. 1(a), and the calculation process of corresponding scale is given the same color in Fig. 1(b), for clearly reflecting the calculation strategy. To overcome the expensive time consuming required for crossing the atomic-scale to meso-scale deformation, two "bridges" are built to connect the simulations at different scales. The first bridge connects atomic-scale and micron-scale: the edge/screw dislocation mobility, atomic strain field induced by lattice distortion and CSRO in HfNbTa RMPEA through MD and MD/MC simulations. By constructing a lattice strain field, the information with material atomic scale is embedded in DDD simulation. Another bridge connects micronscale and meso-scale: by coupling the results of DDD simulations with the CP constitutive model, the material parameters required for CPFE simulation are obtained. Hence, the current models connecting various length scales are established. The coupling strategy between MD simulation and DDD simulation has been discussed and verified in our previous work [24]. In this section, we mainly describe the coupling strategy between the DDD simulations and the CP constitutive model, and determine the necessary parameters that need to be transferred while bridging the different length scales.

The lattice distortion, solid solution and short-range order strengthening are the nonlinear interactions between dislocations and local heterogeneous stress fields induced by different types of atoms in MPEAs. In addition, the local atomic heterogeneous stress fields would affect the obvious evolution of dislocation configuration, and dislocation motion characteristics [10,31,32]. It is widely known that the dislocation movement need break through the resistance from other dislocations and solute atoms. Here, for DDD simulation, RSS on α -slip system would drive dislocation to pass the obstacles from other dislocations and solute atoms during the plastic deformation. Therefore, τ^{α} is expressed as:

$$\tau^{\alpha} = \tau_{p}^{\alpha} + \tau_{sol}^{\alpha} \tag{12}$$

where τ_p^{α} stands for counteracting the interaction between dislocations, and τ_{sol}^{α} corresponds to the stress to overcome the short-range barriers, such as lattice distortion, solid solution, and short-range order [10,31, 32].

Thus, the plastic strain rate from Eqs. (4) and (12) can be modified as:

$$\dot{\gamma}^{\alpha} = \dot{\gamma}_0 sign \left(\tau_p^{\alpha} + \tau_{sol}^{\alpha} - \tau_b \right) \left| \frac{\tau_p^{\alpha} + \tau_{sol}^{\alpha} - \tau_b}{\tau_-^{\alpha}} \right|^{1/m}$$
(13)

and

$$m = \frac{k_B T}{\kappa b^2 r_0 \mu} \text{ and } \dot{\gamma}_0 = \rho_m v_D b^2 \exp\left(\frac{-\Delta Q_s}{T k_R}\right)$$
 (14)

where k_B is the Boltzmann constant, κ is the forest dislocation interaction coefficient, T is the temperature, b is the Burgers vector, r_0 represents the distance to bypass obstacle, μ is shear modulus, ρ_m is the mobile dislocation density, ν_D is the Debye frequency, and ΔQ_s is the slip activation energy. The applied values of m and $\dot{\gamma}_0$ are listed in Table 2, and the evolution of τ^a and $\dot{\gamma}^a$ with the deformation process are obtained from DDD simulations. In this manner, only one parameter τ^a_{sr} is unknown from the left side of Eq. (13). Hence, the evolution of the total slip resistance τ^a_{sr} with simulation time is obtained. The slip resistance τ^a_{sr} on α -slip system is a function of time, therefore, the change rate of slip resistance is quantified. Combined the Eqs. (9)–(11) in the CP model, the change rate of slip resistance $\dot{\tau}^a_{sr}$ is expressed as:

$$\dot{\tau}_{sr}^{\alpha}(t) = \sum_{\beta} |\dot{\gamma}^{\beta}| h_0^{\beta} \left[q_0 + (1 - q_0) \delta^{\alpha\beta} \right] \left| 1 - \frac{\tau_{sr}^{\beta}(t)}{s_s^{\beta}} \right|^{r^{\beta}}$$
(15)

where q_0 is the latent hardening parameter, r^β is hardening exponent, and the applied values of q_0 and r^β are listed in Table 2. Following the previous work [26,30], the hardening parameters of h_0 and s_s have the same value of all slip systems. Hence, the change rate of slip resistance for α -slip system is represented as:

$$\dot{\tau}_{sr}^{\alpha}(t) = h_0 \sum_{\beta} \left| \dot{\gamma}^{\beta} \right| \left[q_0 + (1 - q_0) \delta^{\alpha\beta} \right] \left| 1 - \frac{\tau_{sr}^{\beta}(t)}{s_s} \right|^{r^{\beta}}$$
(16)

Here, the hardening parameters of h_0 and s_s are given the initial values, and the residual of the equation for all slip systems is calculated:

$$R^{\alpha}(t) = \dot{\tau}^{\alpha}_{cr}(t) - h_0 A^{\alpha}(t) \tag{17}$$

with

$$A^{\alpha}(t) = \sum_{\beta} \left| \dot{\gamma}^{\beta} \right| \left[q_0 + (1 - q_0) \delta^{\alpha \beta} \right] \left| 1 - \frac{\tau_{sr}^{\beta}(t)}{s_s^{\beta}} \right|^{\beta}$$
(18)

To compute the minimum residual, Eq. (17) is squared:

$$[R^{\alpha}(t)]^{2} = \left[\dot{\tau}_{sr}^{\alpha}(t)\right]^{2} - 2h_{0}A^{\alpha}(t)\dot{\tau}_{sr}^{\alpha}(t) + h_{0}^{2}[A^{\alpha}(t)]^{2}$$
(19)

Here, the function $f(h_0, s_s)$ is utilized to denote the sum of squares for the residuals in Eq. (19):

$$f(h_0, s_s) = \sum_{\alpha=1}^{12} (R^{\alpha})^2$$
 (20)

Next, the functions $g_1(h_0,s_s)$ and $g_2(h_0,s_s)$ are used to represent the sum of squares of the minimum residuals:

$$g_1(h_0, s_s) = \frac{\partial f(h_0, s_s)}{\partial h_0} = 0, g_2(h_0, s_s) = \frac{\partial f(h_0, s_s)}{\partial s_s} = 0$$
 (21)

In order to obtain the final convergence values for the hardening parameters, the coupled nonlinear differential equations in Eq. (21) are solved using the standard Newton-Raphson program:

$$\begin{pmatrix} h_0 \\ s_s \end{pmatrix}_{k+1} = \begin{pmatrix} h_0 \\ s_s \end{pmatrix}_k - \begin{bmatrix} \frac{\partial g_1}{\partial h_0} & \frac{\partial g_1}{\partial s_s} \\ \frac{\partial g_2}{\partial h_0} & \frac{\partial g_2}{\partial h_0} \end{bmatrix}^{-1} \begin{pmatrix} h_0 \\ s_s \end{pmatrix}_k$$
 (22)

The initial given values for each time node are provided, which obtain the final converged value of hardening parameters of h_0 and s_s . By repeating the above process for each time node, the evolution of hardening parameters with the deformation process is obtained. To verify the rationality of data calibration, the average values of hardening parameters are obtained by limiting the relevant process to the forest hardening stage.

The critical resolved shear stress, s_0 , determines the initial plasticity stage of the mechanical response of CPFE simulation. For the single crystal, s_0 is easily estimated from DDD simulations, and the initial slip resistance of polycrystalline is calculated by measuring the macroscopic yield stress [24,33–35]. Through the above calibration procedure combined with DDD simulations, the material parameters required for CPFE simulation are obtained. It is noted that the material parameters considering the dislocation evolution information would be transferred from small scales to large scales.

3. Basic setup of multiscale simulation

In this section, the basic setup of the multiscale framework with different length scales are introduced. The motion behaviors of edge and screw dislocations in BCC HfNbTa are computed through MD

simulations, material information with CSRO is obtained through MD/MC simulation. Material hardening behavior caused by a large number of dislocation movements is simulated by DDD simulation. The mechanical response of single crystal and polycrystalline HfNbTa RMPEA is simulated by CPFE simulation.

3.1. MD simulation

The applied external force promotes the movement of dislocations in the material and balances the lattice friction, which prevents the dislocation sliding on the slip plane. In BCC materials, the motion behavior of different types of dislocations is significantly different. The speed of edge dislocation is several orders of magnitude faster than that of screw dislocation, because the screw dislocation sliding process requires overcoming the large energy barrier of kink pairs [36].

For this reason, the screw and edge dislocations of the HfNbTa MPEA are simulated by MD simulation, to obtain the dislocation drag coefficient required for DDD simulation. Here, the dislocation mobility of 1/2 $< 111>\{110\}$ edge dislocation and $1/2 < 111>\{110\}$ screw dislocation in the HfNbTa RMPEA is studied (Fig. 2). The MD simulations are performed using an open source LAMMPS software package [37] and visualized using Ovito code [38]. The MD simulations are performed at 300 K. The systems are oriented x-[111], y-[1-10], z-[11-2] for edge dislocation, and x-[11-2], y-[-110], z-[111] for screw dislocation. In order to obtain the convergent dislocation mobility, it is necessary to choose an appropriate simulation box size [39]. The previous work suggests that CRSS converges when the edge or screw dislocation length is longer than 25 nm for two ternary RMPEAs [40,41]. Thus, the dimensions of this sample are 25.5 \times 43.7 \times 14.8 nm³ for the dislocation. The dislocation line length is 25.5 nm, which is larger than 25 nm. The interatomic potential of the simulation cell uses the embedded atomic method potential [42], which is very consistent with various properties of HfNbTa RMPEA, including dislocation behavior under deformation. Energy minimization is performed using periodic boundary conditions along x and y directions and the free boundary condition along z direction. The system is permitted to relax under NVT conditions at room temperature for 100 ps. The position of the dislocation is then monitored as a function of time to follow its movement. Under increasing applied shear load, both screw and edge dislocations experience significant local movement prior to the load at which uninterrupted glide occurs across the simulation box.

The equilibrate of CSRO is performed by MC/MD simulation, which is widely adopted for obtaining the CSRO in MPEAs [17,43]. The samples are set as periodic boundary conditions for three directions, and equilibrated at zero pressure and 300 K under the NPT ensemble. MC steps consist of hybrid MD atomic swaps simulations. Based on the Metropolis algorithm in the canonical system, different types of random atoms are reciprocally interchanged. The samples with different degrees of local ordered structure are obtained by controlling the number of cycles, which include 10 MD steps hybrid with 10 MC swaps. The initial random sample without cycle (OC) of as-cast RMPEA and 500 cycles (5C) of the annealed RMPEA are built. Fig. 3(a) exhibits the atomic structures of HfNbTa RMPEA for different MC/MD cycles (0C and 5C). Here, the Warren-Cowley parameters (WC) are used to describe the degree of local ordered structure in RMPEAs [44], which is expressed as $\alpha_{ii}^n = (P_{ii}^n C_j)/(\delta_{ij}-C_j)$, where *n* represents the *n*-th neighbor shell for *i*-atom, P_{ij}^n is the probability of finding a atom of j-type on the n-th shell, δ_{ij} is the Kronecker delta, and C_i is the content of i-atom of the whole system. It shows a strong segregation of Ta element and a small amount of segregation of Hf element. These observations are in accordance with the previous experimental results that the Ta-rich cluster and Hf-Zr-rich cluster are easier to form in the HfNbTa-based RMPEA [45-47]. The initial random sample has no CSRO, which the parameters of α^1_{ij} are close to zero (Fig. 3b) [48]. The positive values of $a_{\rm Ta-Ta}^1$ and $a_{\rm Hf-Hf}^1$ for 5C sample increase significantly. It means that the degree of local Hf and Ta

Fig. 2. The crystalline orientations of the MD simulation box for screw and edge dislocations.

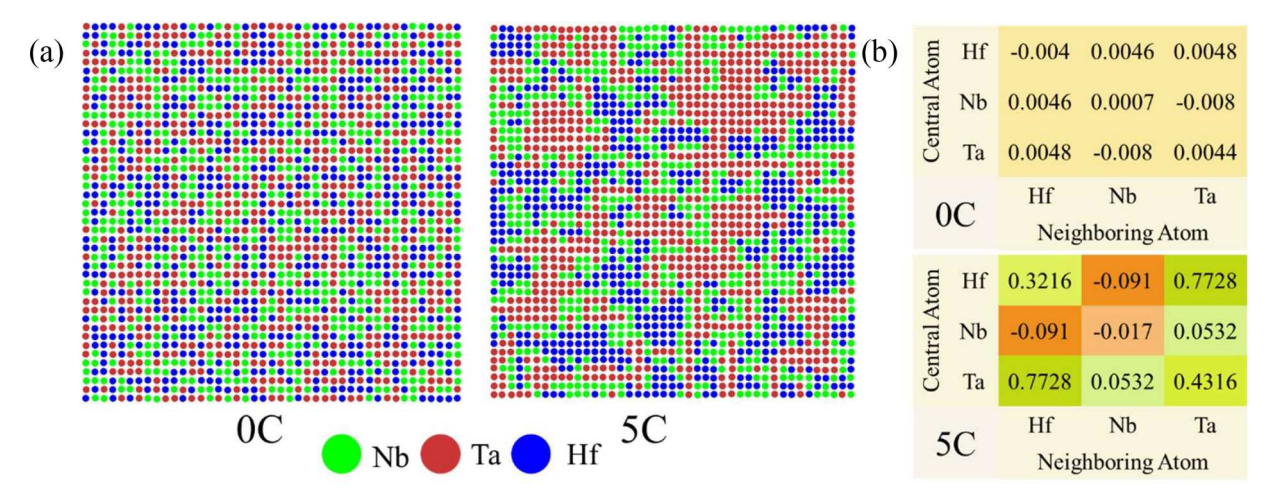


Fig. 3. (a) The atom configurations on the (100) plane is viewed in 0C and 5C samples. **(b)** The average value of the first nearest neighbor pairwise short range-order parameters, a_n^n , in the whole simulation configuration for 0C and 5C samples, where the corresponding samples are described in (a).

segregation increases (Fig. 3b), and α_{Hf-Nb}^1 is a negative value to represent a favorable atomic-pair of Hf-Nb. Next, this model would obtain lattice distortion at the atomic scale in as-cast and annealed RMPEA for the DDD simulation.

3.2. DDD simulation

The essence of multi-scale modeling is to predict the macroscopic mechanical response of materials based on the microscopic physical mechanisms. Since the multiscale models need traverse huge scales from atomic structure to macroscopic mechanical behavior, it is necessary to analyze and model some of the key scales. In this manner, DDD simulation is used as a bridge between the atomic scale single dislocation behavior and mesoscale grain mechanical response.

The ParaDiS program developed by Lawrence Livermore National Laboratory [49], is employed to perform all DDD simulations in current work. Referring to the previous DDD simulations [50], the simulation cell is established with the periodic-boundary conditions, which size is approximately $1.76 \times 1.76 \times 1.76 \ \mu m^3$. The initial dislocation density is set to $\rho_0 \approx 5.5 \times 10^{12} m^{-2},$ according to the experiment [51]. Three dislocation structures constructed, are randomly-distributed edge dislocations, randomly-distributed edge and screw dislocations, and randomly distributed screw dislocations. The material parameters of the HfNbTa RMPEA for DDD simulations are listed in Table 1. Then, the dislocations are evenly distributed on $\{110\}$ slip planes [52] and relaxed without a load condition. The crystal is subjected to the uniaxial tension along [001], [101], [102], [112], [111], [212], [213] orientations [53], and the strain rate is set to $\dot{\varepsilon}$ = $10^4 s^{-1}$ [54].

3.3. CPFE simulation

To explore the plasticity strengthening of HfNbTa RMPEA at the

 $\begin{tabular}{lll} \textbf{Table 1} \\ \textbf{Material} & \textbf{parameters used to simulate the dislocation behavior of HfNbTa} \\ \textbf{RMPEA}. \\ \end{tabular}$

Symbol	Description	Value	Refs.
μ	Shear modulus	42.24 GPa	[25]
V	Poisson's ratio	0.3	[25]
\boldsymbol{A}	Lattice constant	0.3383 nm	[25]
В	Burgers vector	$a\sqrt{3}/2$	[25]
h_k	kink height	$a\sqrt{2/3}$	[25,55]

mesoscale, an open-source finite element code, PRISMS-Plasticity framework [26], is used to perform CPFE simulation, which is built on the deal.II open-source FEM library [56]. The geometry of the CPFE simulation is generated using DREAM.3D package [57]. The open-source code Paraview is used for visualization [58]. The elastic constants for HfNbTa RMPEA are calculated by MD simulations and confirmed in the literature [25]. The flow rule parameters of HfNbTa RMPEA used in the CP model are described in Table 2.

Table 2Material parameters of HfNbTa RMPEA in CP constitutive model.

Parameter	Description	Value	Refs.
C ₁₁	Elastic constant (GPa)	191.12	[25]
C_{12}		128.88	
C_{44}		53.61	
N_{slip}	Total number of slip systems	12	[26,59]
$\dot{\gamma}_0$	Reference strain rate (s ⁻¹)	10^{-3}	[26,60]
m	Sensitivity exponent	0.04	[61,62]
q_0	Self-hardening coefficient	1.4	[29,63]
r	Hardening exponent	1.5	[59,63]

3.3.1. Single crystal

Referring to the previous work [24], a single crystal finite element model is established to capture the tension behavior of HfNbTa RMPEA. The size of the finite element model is $500 \times 500 \times 1500 \ \mu m^3$ with 24, 000 C3D8 (one integration point) 3D-brike finite elements (Fig. 4a). To capture the plastic mechanical behavior of the polycrystalline HfNbTa, seven single crystal orientations locate at the center and edge of the stereographic triangle are set in simulations (Fig. 4b). The specimen is uniaxially stretched along [001], [101], [102], [112], [111], [212] and [213], and the reference frame is x-axis. The single crystals in these seven orientations accurately capture the mechanical response of polycrystals [24]. Keep zero displacement of x-axis at bottom of the finite element model, fix two different nodes at the bottom of the simulation box to avoid rigid body movement, and apply uniaxial tensile displacement along the x-axis direction to the top of the simulation box (Fig. 4c). The sample is uniaxially tensile with a constant stain rate of 10^{-3} s⁻¹ at room temperature. Table 2 shows the constitutive parameter of CPFE simulations.

3.3.2. Polycrystalline

The finite element model has $50 \times 50 \times 50$ hexahedral C3D8 finite elements and containing 200 grains. The model is set to Voronoi tessellation structure (Fig. 5a) and the average grain size is $\sim 18~\mu m$ (Fig. 5b), which is consistent with the experiment [25]. Fig. 5(c) shows the texture of HfNbTa RVE, which is characterized by randomly oriented grains. The load and boundary conditions of the finite element model are shown in Fig. 4(c). For the simplicity, UX, UY, and UZ represent degrees of freedom along the X, Y, and Z axes, respectively. In order to simulate the process of uniaxial tension, UX = 0 on the Y-Z coordinate plane of RVE, UX = UY = UZ = 0 at the position of the coordinate origin, and UZ= 0 at the maximum position of the Y-axis are set. The face of RVE far from the Y-Z coordinate plane is set as the loading face, which applies the variable positive displacement and quasi-static strain rates [24]. In addition, the number of grains and elements of RVE is sufficient to accurately capture the mechanical response of polycrystalline HfNbTa RMPEA in the following section.

4. Computation of hierarchical multiscale model

In this section, the parameters required for different time and length scales of the multi-scale coupling framework are introduced: (i) The edge dislocations and screw dislocations simultaneously existing in the deformation process of BCC HfNbTa MPEA are performed by MD simulations to obtain the input parameters for the DDD simulations. Obtaining atomic strain fields induced by lattice distortion and CSRO through MD/MC simulation; (ii) For the mesoscale CPFE simulation, the

hardening parameters of single crystals with different crystal orientations are calibrated using the decomposition information of each slip system of DDD simulations; (iii) the parameters of single crystals are counted to obtain the input hardening parameters of polycrystalline RVF

4.1. MD to DDD simulations

Fig. 6 shows that the velocity data of edge and screw dislocations at different shear stresses in the HfNbTa RMPEA. For edge dislocations, the dislocation velocity is considered through the phonon damping theory [55]:

$$v_e = b(\sigma - \sigma_c)/B_e \tag{23}$$

where σ is the shear stress, b is the Burgers vector of the dislocation, and B_e is the drag coefficient of edge dislocation, σ_c represents the threshold stress, and dislocations can smoothly glide when $\sigma > \sigma_c$. When $\sigma \leq \sigma_c$, dislocations are pinned by severe energy fluctuations formed by solute atoms, maintaining quiescent states [14,64]. Based on the data fitting in Fig. 6(a), the drag coefficient of edge dislocation is $B_e = 1.0353 \times 10^{-4}$ Pa·s at 300k. For screw dislocation, the dislocation velocity ν_s shows an exponential dependence on stress. It is controlled by the thermal activation process, which is called the kink pair mechanism [17,36]. Based on the previous studies [55,65], the mobility law of dislocation is significantly different in BCC MPEAs. The motion and kink nucleation are defined by an Arrhenius-type form equation [17,55]:

$$v_{s}(\tau,T) = \begin{cases} \frac{\tau b}{B_{s}(\tau,T)} \exp\left(-\frac{\Delta G_{k}}{2K_{b}T}\right) & \text{if } \Delta G_{k} > 0\\ \frac{\tau b}{B(\tau,T)} & \text{if } \Delta G_{k} \leq 0 \end{cases}$$
(24)

Here, the drag coefficient $B_s(\tau,T)$ of the screw dislocation is written as:

$$B_{s}(\tau,T) = \begin{cases} a \left[2a \exp\left(\frac{\Delta G_{k}}{2K_{b}T}\right) + L \right] \\ \frac{2h_{k}L}{B_{0}(T)} & \text{if } \Delta G_{k} \leq 0 \end{cases}$$
 (25)

where $\Delta G_k \left(\tau,T\right) = \Delta H_0 \left\{ \left[1-\left(\frac{\tau}{\tau_0}\right)^p\right]^q - \frac{T}{T_0} \right\}$ is the Gibbs free energy of the kink-pair formation, $T_0 = 0.8T_m$ is a characteristic temperature, T_m is the melting temperature, K_b is the Boltzmann constant, a is the lattice parameter, h_k is the height of the kink at the slip direction, and L is the line length of screw dislocation. The material parameters of the HfNbTa RMPEA are listed in Table 1. The transition of the screw dislocation

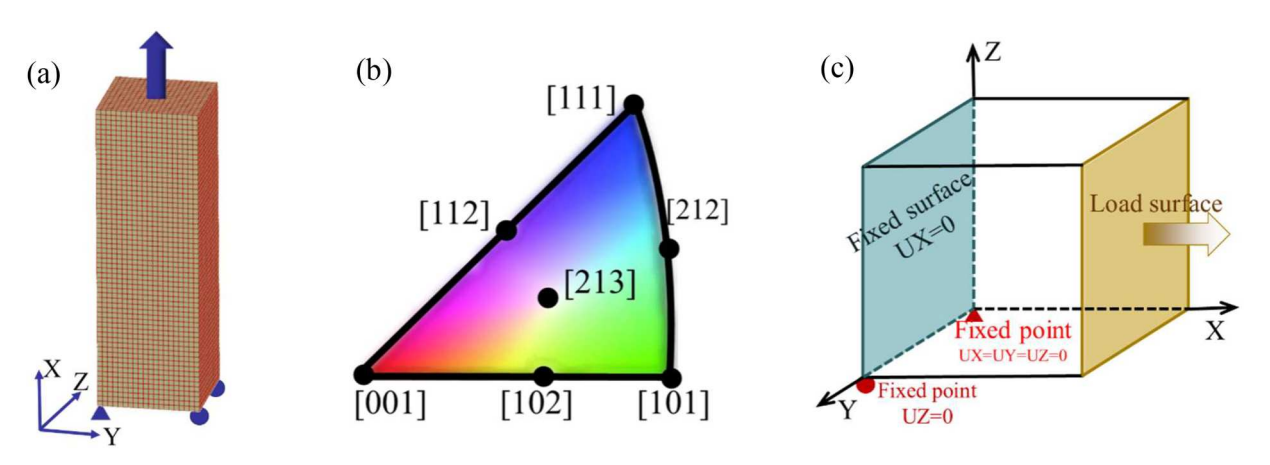


Fig. 4. (a) The finite element model of the single crystal HfNbTa. (b) The different crystallographic orientations at the stereographic triangle. (c) The boundary condition for the single crystal and polycrystal samples.

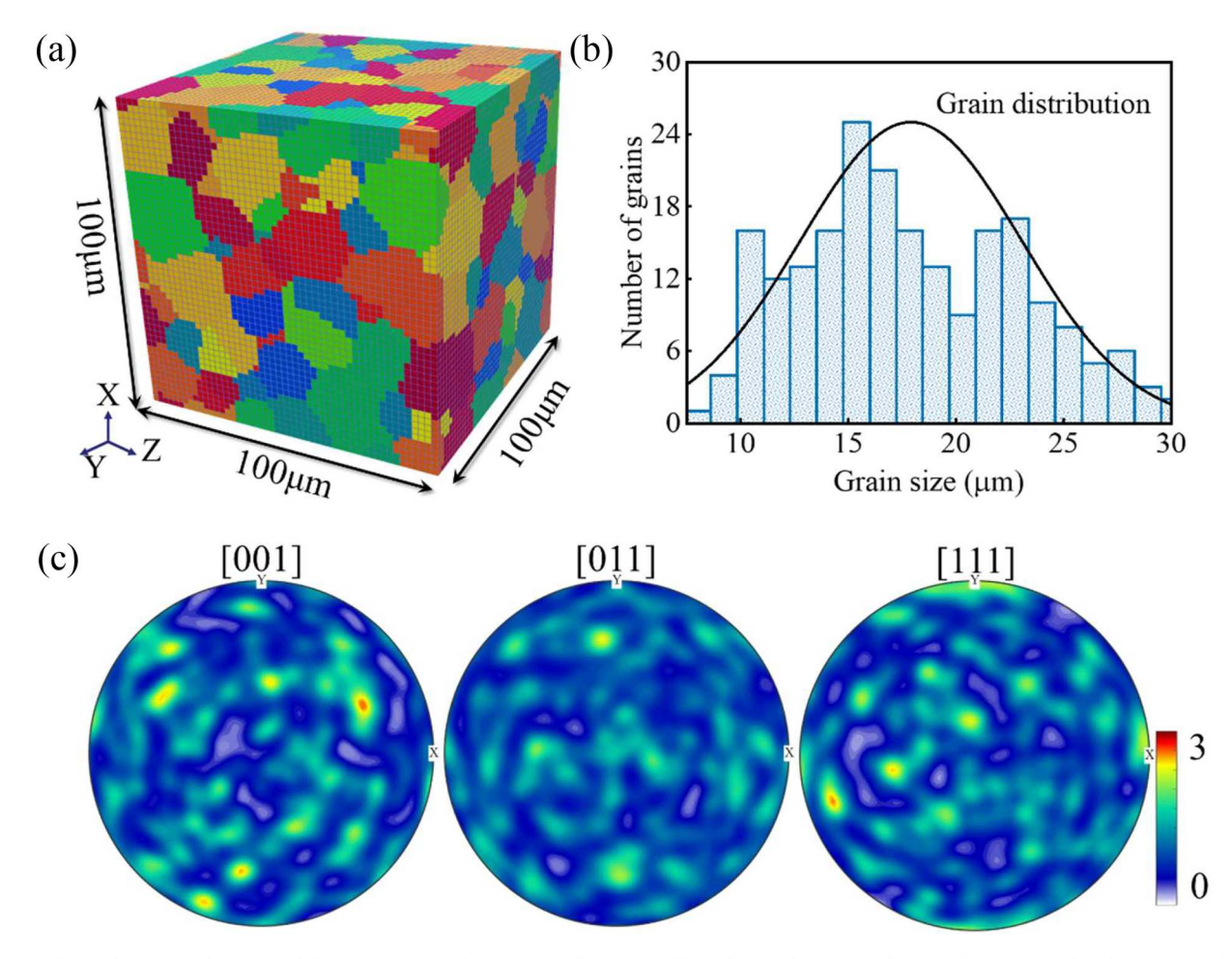


Fig. 5. (a) The HfNbTa finite element model contains 200 randomly oriented grains used by polycrystal CPFE simulations. (b) Grain size distribution of HfNbTa RVE. (c) Representation of initial texture of HfNbTa RVE.

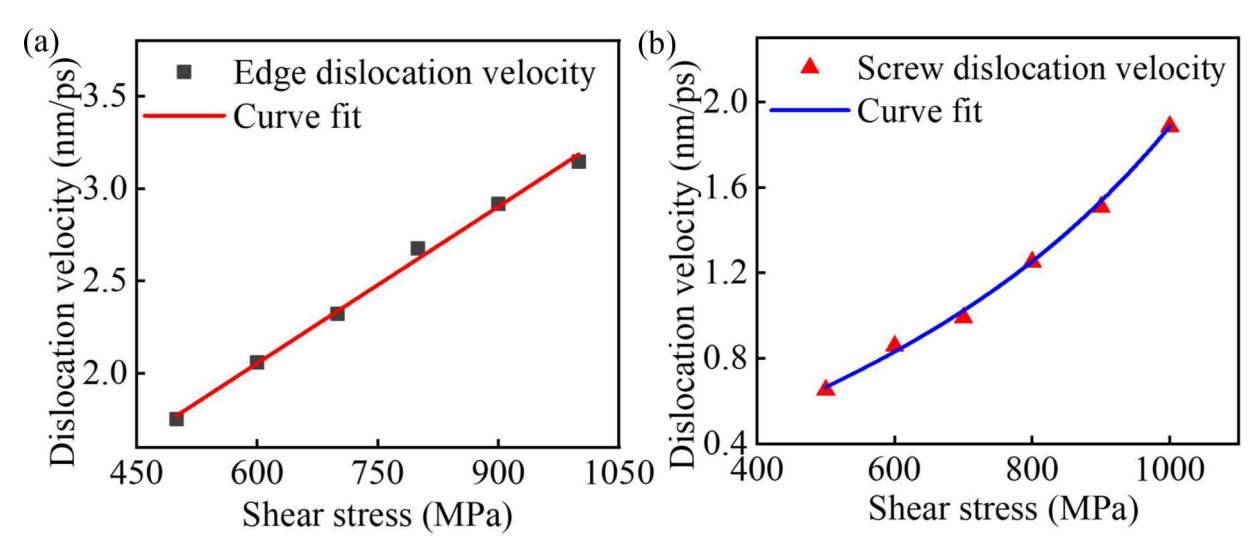


Fig. 6. Dislocation velocity as a function of the applied shear stress for (a) edge and (b) screw dislocations in HfNbTa RMPEA [48].

velocity and drag coefficient is smoothly interpolated by the sigmoidal function with the center of $\Delta G_k = 0$. The sum of the squares of the residuals are minimized by the bounded Fminsearch function in MATLAB to determine the fitting parameters [17]. Based on the data fitting in Fig. 6(b), the parameters of screw dislocation are $B_k = 7.704 \times 10^{-5}$ Pa·s, $B_0 = 4.846 \times 10^{-5}$

The ParaDiS program assumes that the mobility of dislocation is strictly linear, while the mobility of screw dislocation is nonlinear. We have embedded the non-linear mobility law of screw dislocations into the program by modifying the code. A flowchart describing non-linear mobility laws as incorporated into the DDD framework is shown in Fig. 7.

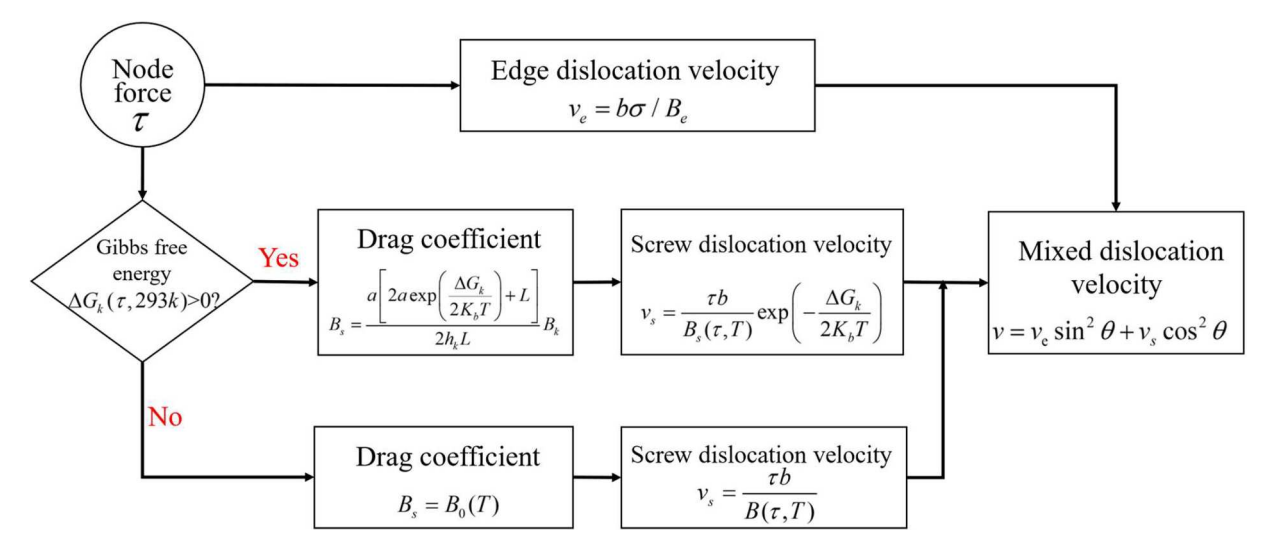


Fig. 7. Flowchart of non-linear mobility laws as incorporated into the DDD framework.

In order to capture the influence of heterogeneous lattice strain field caused by SCRO structure in HfNbTa RMPEA on the strain hardening, a 3D lattice strain field is developed and embedded into the DDD simulation. The strain field, $\sigma_{ij}(x)$, caused by local ordered structure is obtained by atomic displacement from MD simulations. The volumetric strain, $\theta = \varepsilon_{xx} + \varepsilon_{yy} + \varepsilon_{zz}$, obtained by MD simulation is compared with the theoretical volumetric strain (Fig. 8a, b), verifying the accuracy of the strain field. According to the geometric model, the volumetric strain of the atom, i, in HfNbTa RMPEA is obtained from Fig. 8(b) [66]:

$$\theta_{i} = \frac{\sum_{j=1}^{n} \omega_{ij} C_{j}}{\sum_{k=1}^{n} A_{ik} c_{k}} - \frac{4\pi \overline{\eta}}{N_{i} \sum_{k=1}^{n} A_{ik} c_{k}}$$
 (26)

where C_j is the probability of the j atom at the nearest neighbor of the central atom i. Based on the atomic configuration and coordinates obtained from MD simulation, we perform the same calculation on the lattice points where each i atom is located, that is, calculate the proportion of j atoms among the 8 closest atoms of i atom. c_k is the atomic fraction of the k atomic, the space angle occupied by the j atom relative to the central atom i is $\omega_{ij} = 2\pi[1 - \sqrt{r_i(r_i + 2r_j)}/(r_i + r_j)]$, the average

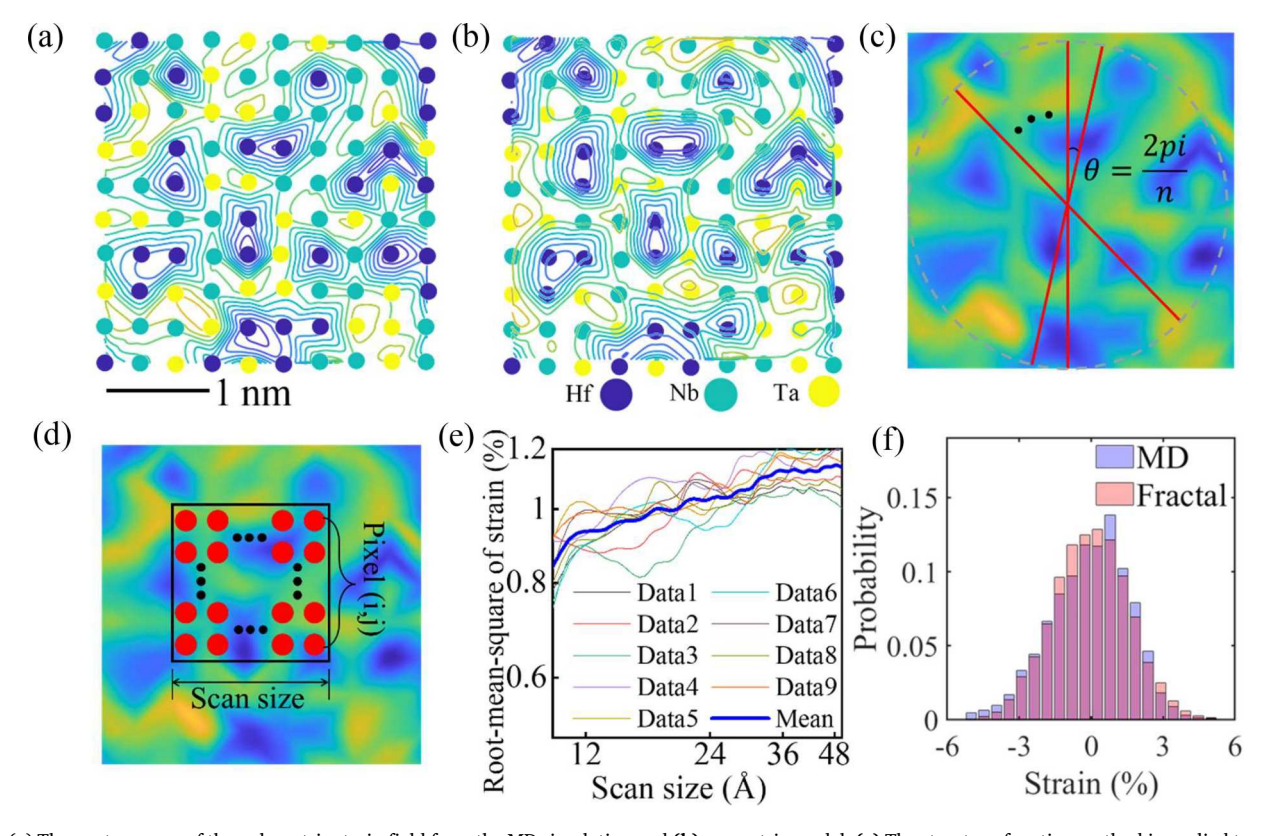


Fig. 8. (a) The contour map of the volumetric strain field from the MD simulation and (b) geometric model. (c) The structure-function method is applied to calculate fractal dimensions and strain amplitude. (d) Root-mean-squared strain is obtained by strain field. (e) The root-mean-square of the strain vs scan size in the log-log plot. Here, data 1–6 are obtained from the strain on the different sections. (f) The statistical results of the normal strain obtained by the MD simulation and fractal function.

atomic arrangement density is $\bar{\eta} = 1/2\sum_{i=1}^n\sum_{j=1}^n c_i c_j N_i [1 - \sqrt{x_{ij}(x_{ij}+2)}/(x_{ij}+1)]$, N_i is the coordination number of the central atom, $x_{ij} = r_i/r_j$ is the ratio of radius, r_i is the radius of the i atom, and $A_{ik} = 2\pi x_{ij}/[(x_{ij}+1)^2\sqrt{x_{ij}(x_{ij}+2)}]$.

Considering the stress field induced by lattice distortion is the main hindering/driving effect for dislocation movement in MPEAs. Hence, as with previous theoretical work [67], the stress field induced by elastic strain is introduced into the DDD simulation, to explore plastic behavior caused by large-scale dislocation motion in MPEAs. Through statistical analysis of discrete atomic strains, the relationship between root-mean-squared strain, $S_q = \sqrt{\langle \sum_{i=0}^{Nx-1} \sum_{j=0}^{Ny-1} (\varepsilon(i,j) - \overline{\varepsilon})^2 \rangle}$, and scan size shows a power-law (Fig. 8d, e). It indicates the fractal characteristic of HfNbTa RMPEA [68]. Here, $\overline{\varepsilon}$ is the average strain. $N_x = 100$ and $N_y = 100$ are the pixel numbers along x and y, respectively. $\varepsilon(i,j)$ is the strain in the pixel, (i, j), and $\langle \cdot \cdot \cdot \rangle$ is the average. According to 2D Weierstrass-Mandelbrot fractal method, a 3D fractal strain-field function is developed to capture the strain of HfNbTa RMPEA [32,69]:

$$\varepsilon\left(\mathbf{r}\right) = \mathbf{H}^{\mathrm{D}-3} \left(\frac{\ln \gamma}{M}\right)^{\frac{1}{2}} \sum_{m=1}^{M} \times \sum_{n=0}^{n_{\mathrm{max}}} \left[\cos\left(\phi_{m,n}\right) - \cos\left(\frac{2\pi \gamma^{n} \overrightarrow{n}_{m} \cdot \mathbf{r}}{L} + \phi_{m,n}\right)\right] \left(\frac{\gamma^{n}}{L}\right)^{\mathrm{D}-4}$$
(27)

where $\left(\frac{\ln y}{M}\right)^{\frac{1}{2}}$ is the normalizing factor, and \overrightarrow{n}_m is unit vectors uniformly distributed at the 3D hypersphere. We obtain uniformly distributed coordinates of m points on a sphere with a radius of 1. These points generate m unit vectors \overrightarrow{n}_m from the origin of the center of the ball), and the $M \times n_{\max}$ random phases $\phi_{m,n}$ are randomly distributed between 0 and 2π , $\phi_{m,n}$ is the random phase, and $n_{\max} = \inf[\log(L/L_s)/\log \gamma]$. Here, $L_s = 4$ b is a cut-off size, L is sample size, and int [...] is used to obtain the maximum integer value. $\gamma = 1.5$ controls the frequency density, and M = 50 is applied to control the profile [48].

H and D are strain amplitude and fractal dimension (Fig. 8c), which are obtained by a log-log plot of horizontal length (L_{hori}) vs. structure-function [$S(\tau_x,\tau_y)=\langle (z(x,y)-z(x+\tau_x,y+\tau_y))^2\rangle$] [70]. Here, $\tau_x=L_{hori}\cos\theta$, and $\tau_y=L_{hori}\sin\theta$. z(x,y) is the strain in the pixel (x,y). $\theta=\frac{2\pi}{n}$, ... 2π (n=50 in this work) is used to build n profiles derived from the image. The structure-function obeys the approximate scaling law $S(L_{hori})=\Lambda(L_{hori})^{2(2-D_S)}$, where $D_p=\frac{4-T_S}{2}$ is the profile fractal dimension. The strain amplitude parameter is $H=\exp\{\ln\Lambda+\ln\{2\Gamma(5-2D_p)sin[(2-D_p)\pi]\}-\ln\pi\}/(2D_p-2)$. Here, $\Gamma(x)$ is the gamma function. Ts and $\ln(\Lambda)$ are the slope and intercept of a log-log plot of S vs. L_{hori} . The surface fractal dimension is $D_{SF}=\langle D_p\rangle+1$. The fractal dimension of the 3D strain field is $D=D_{SF}+1$. The D and H are listed in Table 3. The statistical strains show the strain-field mapping acquired by a fractal function is consistent with the MD simulation from the perspective of numerical value (Fig. 8f).

The correlation between different atomic strain components from MD simulation is discussed by calculating the Pearson correlation coefficient [71]:

$$r = \frac{\sum_{i=1}^{n} (X_i - \overline{X})(Y_i - \overline{Y})}{\sqrt{\sum_{i=1}^{n} (X_i - \overline{X})^2} \sqrt{\sum_{i=1}^{n} (Y_i - \overline{Y})^2}}$$
(28)

When $\mid r \mid <=0.3$, there is no correlation; $0.3<=\mid r \mid <=0.5$ shows the low degree relationship [68]. The absolute values of the Pearson correlation coefficient between different strain components are less than or close to 0.3, indicating a weak correlation between strain components (Tables 4, 5). Therefore, the field functions of different strain components are independent of each other.

According to the generalized Hooke's law, the stress field caused by lattice distortion in MPEA is obtained:

$$\sigma_{ii}^{mpea} = 2G\varepsilon_{ii} + \lambda\varepsilon_{kk}\delta_{ii} \tag{29}$$

The total stress is calculated by composing the load stress of σ^{ext} , the stress caused by dislocation of σ^{disl} , and the stress dominated by locally ordered structure of σ^{mpea} . The f_{ij}^{PK} depend on the local stress on the segment acting on the dislocation segment, ij:

$$f_{ij}^{PK} = \left[\sigma^{ext} + \sigma^{disl} + \sigma^{mpea}\right] \cdot \mathbf{b}_{ij} \times \mathbf{t}_{ij}$$
(30)

where the σ^{ext} and σ^{disl} are calculated by the DDD simulation. The stress, σ^{mpea} , of lattice strain field dominated by locally ordered structure in RMPEAs is obtained from the 3D fractal strain-field function. \mathbf{b}_{ij} is Burgers vector, and \mathbf{t}_{ij} is the unit vector parallel to the segment, ij. The node velocity of the dislocation segment can be expressed as:

$$\mathbf{v}_{ij} = \frac{f_{ij}^{PK}}{B(\tau, T)} \tag{31}$$

When dislocation lines slip in RMPEAs, the non-uniform strain field caused by CSRO will hinder/promote dislocation movement, causing an increase/decrease in dislocation velocity.

4.2. DDD to CPFE simulations

The behavior of a large number of dislocations is calculated by DDD simulation. Fig. 9(a) shows the distribution of screw and edge dislocations in the HfNbTa RMPEA with local ordered structure, as well as the dislocation configurations on different slip planes. Due to severe lattice distortion from CSRO, high strain fluctuations occur on the dislocation slip plane, causing the multiple cross slip. Therefore, a large number of cross kinks are observed in plastic deformation stage (Fig. 9b), controlling the dynamics evolution of screw dislocations [72–74]. This

Table 4The Pearson correlation coefficient for different atomic-strain components from MD simulation without CSRO.

	ϵ_{xx}	ϵ_{yy}	ϵ_{zz}	ϵ_{xy}	ϵ_{xz}	ϵ_{yz}
ε_{xx}		0.311	0.293	-0.006	-0.015	0.011
ϵ_{yy}	0.311		0.327	-0.005	-0.004	-0.001
ϵ_{zz}	0.293	0.327		0.023	0.014	0.008
ϵ_{xy}	-0.006	-0.005	0.023		0.02	-0.008
ϵ_{xz}	-0.015	-0.004	0.014	0.02		-0.017
ϵ_{yz}	0.011	-0.001	0.008	-0.008	-0.017	

Table 3 The fractal dimension, D_{ij} , and strain amplitude, H_{ij} , for the strain components, ε_{ij} of the HfNbTa RMPEA based on MD results [48].

Strain components		ϵ_{xx}	$\epsilon_{ m yy}$	ϵ_{zz}	ϵ_{xy}	ϵ_{xz}	ϵ_{yz}
Fractal dimension, Dij		D_{xx}	D_{yy}	D_{zz}	D_{xy}	D_{xz}	D_{yz}
-	0C	3.8217	3.8256	3.8234	3.8437	3.8309	3.8364
	5C	3.6907	3.6812	3.6882	3.7348	3.7451	3.7309
Strain amplitude,		H_{xx}	H_{yy}	H_{zz}	H_{xy}	H_{xz}	H_{vz}
$H_{ij} (\times 10^{-4})$	0C	12.3583	12.2712	11.87	14.7458	13.6489	14.0585
•	5C	5.6745	5.3889	5.8362	8.4178	8.9782	8.4209

Table 5The Pearson correlation coefficient for different atomic-strain components from MD simulation with CSRO.

	ε_{xx}	ϵ_{yy}	ϵ_{zz}	ϵ_{xy}	ϵ_{xz}	ϵ_{yz}
ϵ_{xx}		0.07	0.041	0.048	-0.002	0
ε_{yy}	0.07		0.108	0.013	0.01	0.005
ϵ_{zz}	0.041	0.108		0.023	-0.016	-0.043
ε_{xy}	0.048	0.013	0.023		0.031	0.005
ϵ_{xz}	-0.002	0.01	-0.016	0.031		0.006
ϵ_{yz}	0	0.005	-0.043	0.005	0.006	

phenomenon in the HfNbTa RMPEA is consistent with the dislocation configuration in the BCC RMPEA from the previous study [72].

In HfNbTa RMPEA, the slip plane of dislocations deviates from the standard BCC slip plane due to the severe lattice distortion, such as the {134} slip plane (Fig. 10), which is consistent with previous experimental observations [75]. This result indicates that the non-uniform strain field induced by lattice distortion has a significant impact on the dislocation motion behavior, inducing unusual dislocation. Here, this trend is captured by DDD simulations.

Fig. 11 shows the evolution of the total plastic shear strain in HfNbTa RMPEA along [001] orientation as an example. The relationship

between the plastic shear strain rate and the resolved plastic strain rate is expressed as:

$$\dot{\varepsilon}_p = \sum_{\alpha=1}^N \dot{\gamma}^\alpha S_\alpha \tag{32}$$

where S_{α} is the Schmid factor of α -slip system. The initial time, the part before $t=t_{\rm r}$ corresponds to the relaxation of the initial microstructure, and then the total plastic shear strain increases linearly with the time (Fig. 11). The slope is used to describe the plastic-shear strain rate. Therefore, the strain rate applied by DDD simulation during plastic deformation is balanced with the total shear strain rate. It is important to note that the total plastic-shear strain rate generated from Fig. 11 is close to the load strain rate.

The calculated parameters from DDD simulations present fluctuate with the time, so the extraction of hardening parameters of CPFE model should go through the time average of the calibration program. The average period selected should ensure that the mechanical response of the single crystal in DDD simulation is not affected by the transients caused by the relaxation of the initial configurations. Forest hardening is widely used to determine the strength of interaction between dislocations [76,77], the RSS of forest hardening conforms to Taylor law:

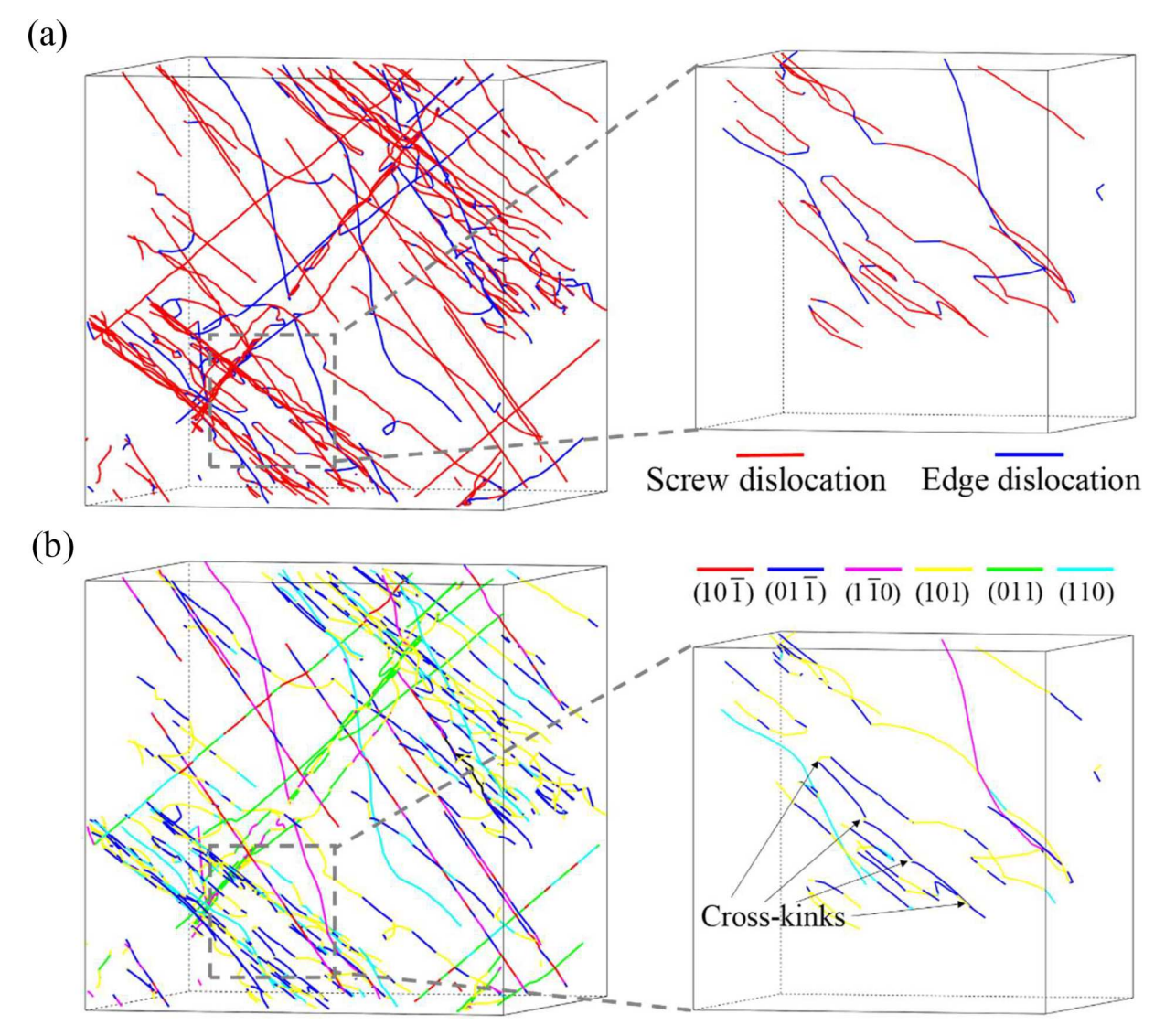


Fig. 9. (a) The screw and edge dislocation configuration along [100] crystal orientation, and (b) the dislocation configuration colored by different slip planes at the strain of 0.8 %.

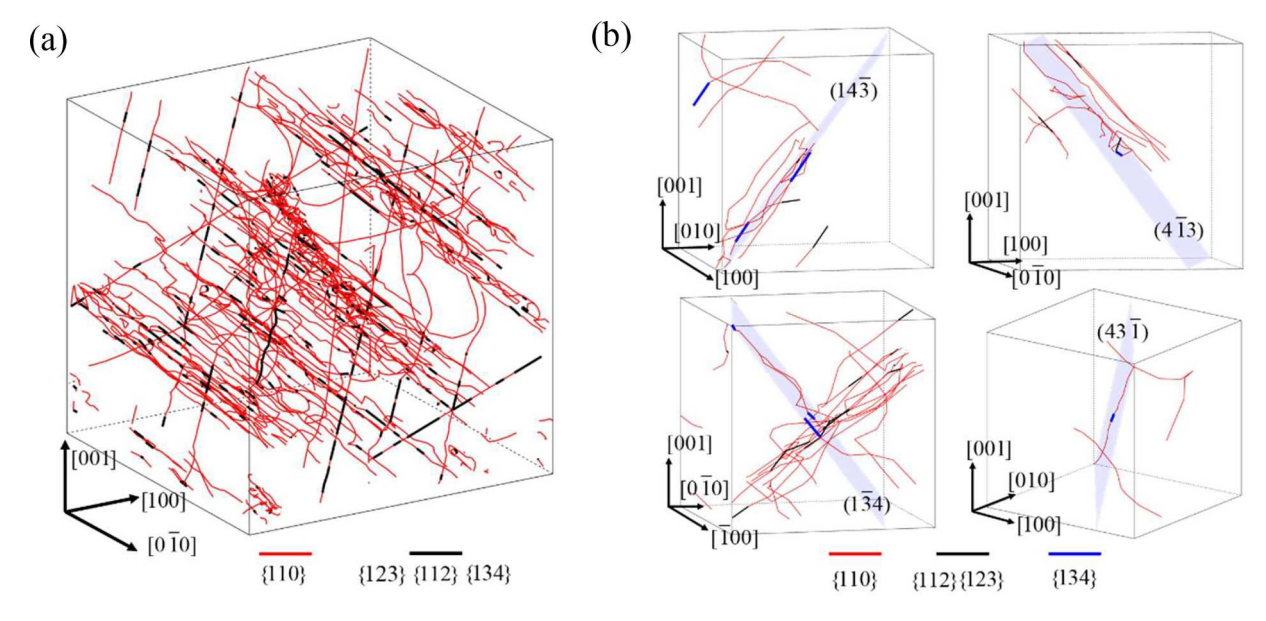


Fig. 10. (a) The dislocation structure colored by different slip planes at the strain of 1 % alone [100] direction. (b) is the enlarged view of (a).

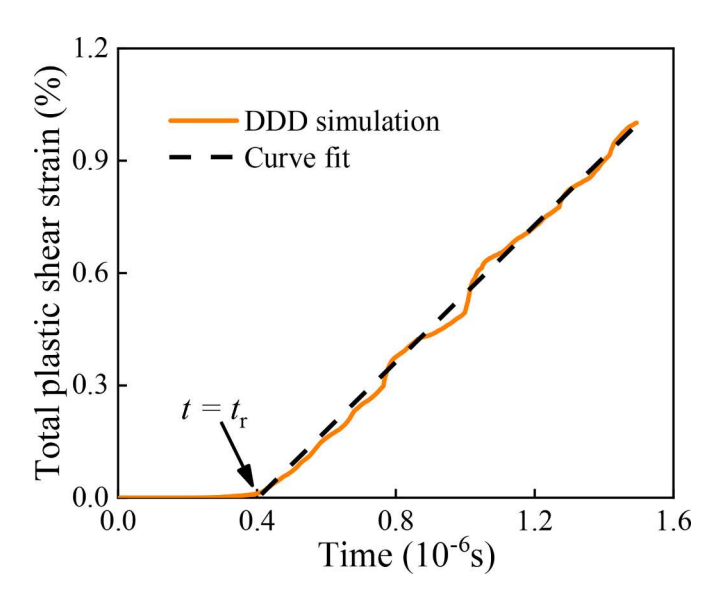


Fig. 11. The evolution of the total plastic shear strain as a function of time in HfNbTa RMPEA from DDD simulations.

$$\tau = bk\mu\sqrt{\rho} \tag{33}$$

where k is the interaction coefficient, and reflects the strengthening of the dislocation junction in forest network.

Fig. 12 shows the stress-strain curves and the evolution of k with time for HfNbTa RMPEA along [001] crystallographic orientation. As a comparison, the results of classic alloy (without the lattice distortion, other parameters remain unchanged) are presented in the Fig. 12. The parameter k rises to the peak, and then decreases to fluctuating slightly near a constant value (the red solid line). The evolution curve is divided into two time periods by a black solid line. In the transient region (between 0 and t_0), the initial dislocation structure does not match the loading deformation rate and begins to recombine and proliferate with the increase of strain; from the second region, the current dislocation is in the forest hardening state and matches the strain rate of the material after the dislocation structure is reconstructed. In Fig. 12(a), the strength of as-cast HfNbTa is much higher than that of classical alloys, because the high friction stress caused by lattice distortion hinders dislocation

movement to enhance the strength. The decomposition shear stress in MPEAs is higher than that in traditional alloys for the same dislocation structure, therefore, the interaction coefficient of as-cast HfNbTa RMPEA in Fig. 12(b) is higher than that of classic alloys [78]. It is worth noting that locally ordered structure further enhances the strength of as-cast HfNbTa (Fig. 12a), and the interaction coefficient 1.53 in the annealed HfNbTa is higher than 1.35 in the as-cast HfNbTa (Fig. 12b). Although the strain is lower in the segregation region of a single element, the segregation of an element lead to an increase in the binding of other elements. This results in high lattice strain at the edge of the element enrichment region [10], further increasing the strain gradient and generating strong strain fluctuations. Thus, the existence of CSRO structure causes strong strain gradient and strain fluctuations to hinder the dislocation slip, improve the strength of RMPEA.

The calibration of the hardening parameters of the CP model should be limited to ensure that the obtained hardening parameters are not affected by the transient region. The CP hardening parameters are calibrated after the initial time of forest hardening state. It also ensures that the hardening parameters accurately predict the mechanical response of single crystals with different crystal orientations. After obtaining the smooth region of dislocation hardening parameter evolution with different crystal orientations, the saturation slip resistance and initial hardening parameter are calibrated using the hierarchical multiscale crystal plasticity model in Section 2.2. Here, the hardening parameters of s_s and h_0 as a function of time are presented in Fig. 13. In the transient region, the values of hardening parameters converged by the calibration program are less and have obvious fluctuate. In the forest hardening state $(t > t_0)$, the hardening parameters are almost stable to a constant value over time. The extraction of initial resolved slip resistance for different crystallographic orientations in CPFE model is obtained based on the stress-strain curves of DDD simulations. Due to the obvious fluctuation of DDD simulations, the first deviation from formal linearity, 0.02 % offset yield and 0.04 % offset yield are extracted, and then averaged and multiplied them by Schmid coefficient of different loading orientations [24]. The hardening parameters of single crystals of the as-cast and annealed HfNbTa RMPEA with different loading orientations are listed in Table 6 and Table 7, respectively. Then, they are applied to the CP model to capture the mechanical behavior of HfNbTa RMPEA at mesoscale.

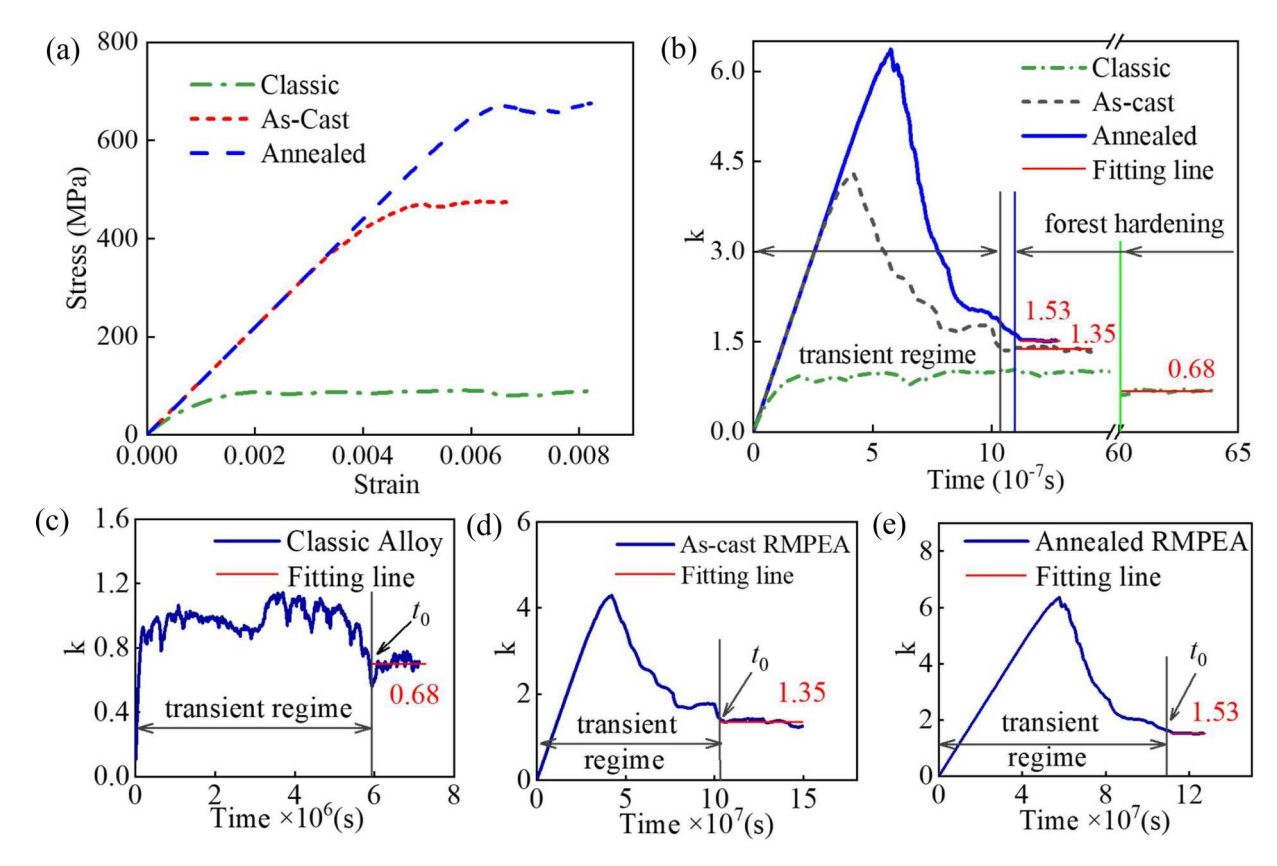


Fig. 12. (a) The stress-strain curves of DDD simulations along [001] crystallographic orientation, and (b) the variation of dislocation interaction coefficient with time in the (c) classic alloy, (d) as-cast HfNbTa RMPEA and (e) annealed HfNbTa RMPEA along [001] crystallographic orientation.

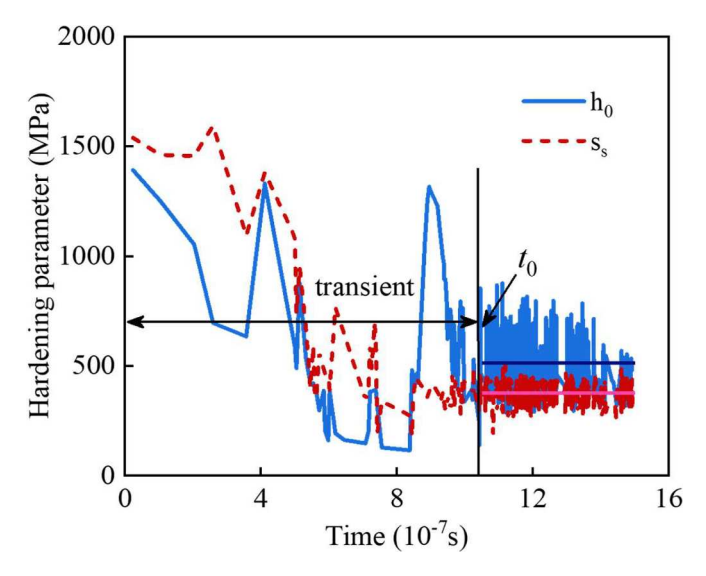


Fig. 13. Evolution of hardening parameters of as-cast HfNbTa RMPEA along [001] load orientation with time. The horizontal line represents the extracted average value of parameter after the initial time.

Table 6
Hardening parameters of CP model from DDD simulations for different single crystallographic orientations of as-cast HfNbTa RMPEA.

Orientation	[001]	[101]	[102]	[111]	[112]	[212]	[213]
s ₀ (MPa)	203.6	247.1	224.5	262.0	258.1	212.3	290.5
h_0 (MPa)	515.6	348.1	456.4	563.8	428.6	490.3	435.1
s_s (MPa)	375.6	302.5	299.3	397.5	323.4	285.7	324.1

Table 7Hardening parameters of CP model from DDD simulations for different single crystallographic orientations of annealed HfNbTa RMPEA.

Orientation	[001]	[101]	[102]	[111]	[112]	[212]	[213]
s ₀ (MPa)	285.7	338.8	384.6	266.7	322.2	289.6	312.8
h_0 (MPa)	586.1	401.4	593.3	670.5	525.8	595.2	644.4
s_s (MPa)	434.2	410.1	509.2	414.5	353.1	311.6	394.8

4.3. Monocrystalline to polycrystalline simulations

Because it is time-consuming and difficult to conduct authoritative experiments on the mechanical responses of single crystals with various orientations, it is still necessary to determine the number of single crystal orientation, which is used to simulate the mechanical behavior of polycrystals. The previous work demonstrates that the mechanical response of polycrystalline materials is accurately quantified using the hardening parameters calibrated with the seven single crystal orientations ([001], [101], [111], [102], [112], [212] and [213]) [24,53]. The boundary conditions of grains in polycrystalline RVE are more complex than that in single crystal, so CRSS cannot be characterized by the simple average value of single crystal. The yield stress with the Taylor factor is used to quantify CRSS in polycrystalline RVE [33]. Here, CRSS of the as-cast HfNbTa RMPEA is 310.3 MPa, and that of the annealed HfNbTa RMPEA is 356.7 MPa [79].

After the hardening parameters of single crystals in seven orientations are calibrated in the Section 4.2, the relationship between them is established. It is found that when the hardening parameter is taken as a random variable, it presents an approximate normal distribution. Fig. 14 shows the distribution histogram of hardening parameters in seven orientations of as-cast and annealed HfNbTa RMPEA. The saturated slip resistance is 329.74 MPa and 399.94 MPa in the as-cast and annealed

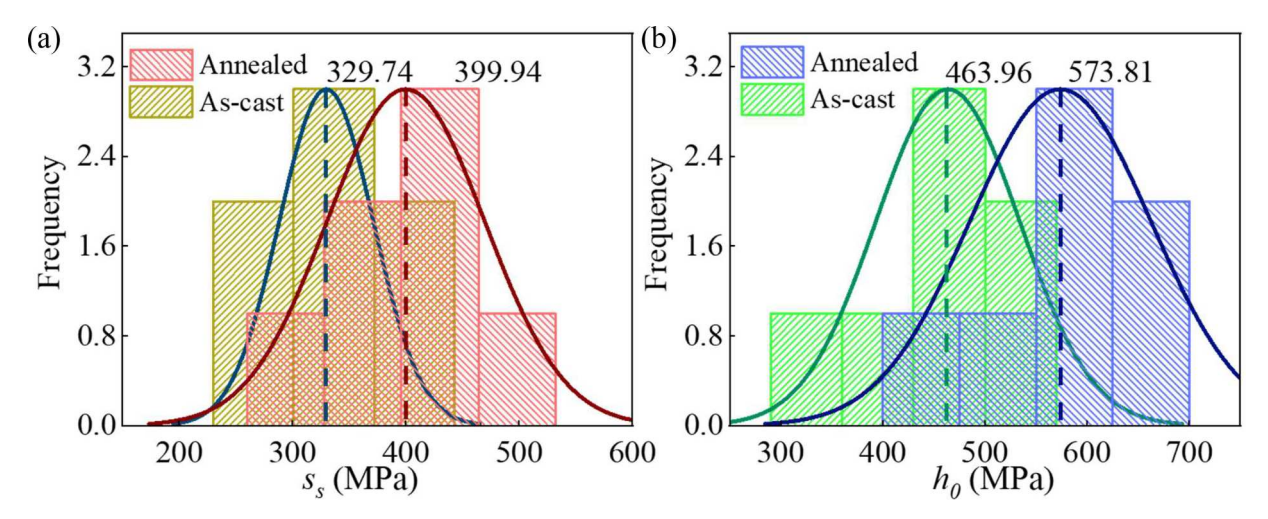


Fig. 14. Distribution histogram of CP hardening parameters of single crystal in seven orientations in the (a) as-cast and (b) annealed HfNbTa RMPEA. The dotted line is the average value of hardening parameters.

polycrystalline HfNbTa RMPEAs, respectively. The corresponding initial hardening modulus is 463.96 MPa and 573.81 MPa. The increase of hardening parameters usually leads to the high strain hardening rate in the MPEA [24,53]. Thus, the average value of the hardening parameters in the CPFE model is obtained, and then would be used to predict the mechanical response of polycrystalline HfNbTa.

5. Deformation and strengthening behavior

In this section, the results for deformation and strengthening of the HaNbTa RMPEA at the mesoscale CPFE simulations are presented. Meanwhile, the model is verified. In Section 5.1, the tensile results of single crystal models in different orientations are compared with the DDD simulations. In Section 5.2, the mechanical response of polycrystalline RVE in uniaxial tension of as-cast and annealed HfNbTa are analyzed.

5.1. Single crystal plasticity

Based on the hardening parameters of different single crystal orientations from small length scale, the CPFE method at the mesoscale is performed to simulate the mechanical response of the single-crystal HfNbTa under the uniaxial tension. Fig. 15 exhibits a comparison of tensile stress-strain curves in the as-cast and annealed HfNbTa along seven crystallographic orientations, including [001], [101], [102], [111], [112], [212] and [213]. Compared with the [111] orientation, the strain hardening rates in other orientations are closer to the [001]-

[101] symmetry axis in the stereographic triangle. The yield strength along [111] orientation is the highest, and the corresponding value of the as-cast and annealed HfNbTa RMPEA is 968.2 MPa and 986.2 MPa (Fig. 15). The magnitude of Schmid factor affects the shear stress required for dislocation activation. The various dislocation growth rates between single crystal orientations lead to the difference of strain hardening rate. Table 8 shows the Schmid factor for different orientations, the smallest Schmid factor of 0.27 at the [111] orientation in HfNbTa. This trend proves that the stress-strain curve of [111] orientation has the highest slope. The crystal orientation with small Schmid factor has a strong strain hardening [24]. The difference of the strain hardening behavior in the single crystal BCC materials has been widely studied [80,81]. Additionally, the current work focuses on the effect of CSRO on the mechanical response in HfNbTa, and these aspects of the differences between single crystals would not be discussed in more detail

Except for the [111] orientation, the yield strength of the other orientations in the single crystal annealed HfNbTa is changed between 685.0 MPa and 839.7 MPa. The yield strength in the annealed sample is about 214.6 MPa higher than that of the as-cast HfNbTa between 448.1

Table 8The Schmid factor of various orientations.

Dislocation slip	Loading	direction	1				
system	[001]	[101]	[111]	[102]	[112]	[212]	[213]
Schmid factor	0.41	0.41	0.27	0.49	0.41	0.41	0.47

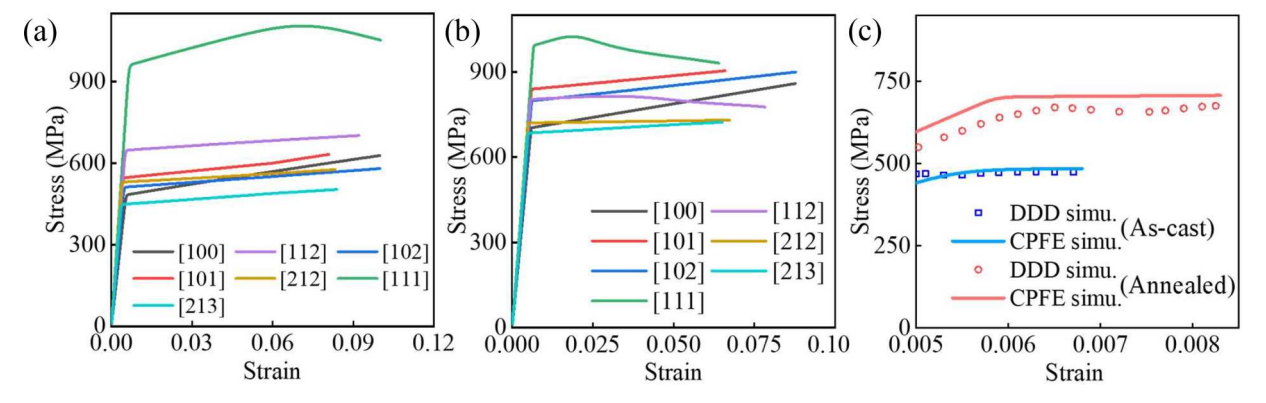


Fig. 15. The strain-stress curves for the single crystal of seven crystallographic orientations in the (a) as-cast and (b) annealed HfNbTa. (c) Comparison of stress-strain curves predicted by DDD simulation and CPFE simulation along [100] crystallographic orientation.

MPa and 647.3 MPa (Fig. 15a, b). The [111] orientation of annealed sample shows more obvious softening than that of as-cast sample (Fig. 15a, b). The existence of CSRO advances the strain at the stress strain inflection point in the [111] orientation (0.07 to 0.019). In addition, the [112] orientation of annealed HfNbTa also shows the softening phenomenon. Thus, the existence of CSRO greatly improves the yield strength of the annealed sample, and reduces the difference in the mechanical response of various single crystal orientations. Fig. 15(c) compares the stress-strain response predicted by DDD simulation and CPFE simulation along the [001] crystal orientation. The results indicate that the stress-strain curves predicted by CPFE simulation are in good agreement with DDD simulation in the as-cast HfNbTa. The error of the predicted stress-strain curve of annealed sample is within 10 %, with the maximum error occurring near the yield point.

5.2. Polycrystal plasticity

Generally, the number of elements and grains is crucial to the CPFE simulation. Too few elements lead to the inaccurate calculation, otherwise, it wastes the computing resource and time. Meanwhile, too few grains would not accurately represent the mechanical response of polycrystalline materials. In order to accurately capture the mechanical response of polycrystalline RMPEA and without wasting computing resource, the appropriate element number and grain number of polycrystalline RVE should be obtained in advance. Here, RVE with different grain numbers (30, 50, 100, 200 and 300) is established, and the uniaxial tensile simulation is conducted under the same boundary conditions. The grain orientations of all models are random (Fig. 16a). The stress-strain curves of polycrystalline models with different grain numbers are presented in Fig. 16(b). With the increase of the number of

grains, the stress-strain curve gradually approaches the same value. The stress level predicted by RVE for 30 grains is too high due to the more inclined orientation (Fig. 16a), and the predicted stress-strain curves of 200 and 400 grains are almost identical. Fig. 16(c) shows the stress-strain response of RVE containing 200 grains and different element numbers. The result shows that the RVE with 125,000 elements (50 \times 50) can represent the mechanical response of the polycrystalline RMPEA. Therefore, The RVE with 200 grains and 125,000 finite elements would predict accurately the mechanical behavior of the polycrystalline HfNbTa.

Fig. 16(d) shows the stress-strain curve of polycrystalline RVE in uniaxial tension of as-cast and annealed HfNbTa. To verify the accuracy of the developed CPFE approach, the experimental results are compared [25]. Fig. 16(d) reveals that the simulated result of the as-cast polycrystalline HfNbTa is good agreement with the experimental result. At the yield point of the curve, the CPFE simulation shows the insufficient prediction. The experimental result shows the bilinear characteristics, while the simulation shows a smooth transition of the gradually accumulated slip strain near the yield point. The yield point of the annealed HfNbTa is 132.3 MPa higher than that of the as-cast sample. The local ordered structure hinders the cross-slip and reduces the double-kink nucleation rate of the screw dislocations, resulting in high strength of MPEA [11,12].

Fig. 17 shows the distribution of the $\langle 100 \rangle, \langle 110 \rangle$, and $\langle 111 \rangle$ pole figure after the uniaxial tension. Compared with the undeformed sample (Fig. 5), only a small area with higher density appears on the (100), (110), and (111) planes. The maximum intensity value is 1.6 after deformation in Fig. 17, which is smaller than 2.5 before deformation in Fig. 5. Thus, there is no obvious texture after the plastic deformation. As the deformation continues, the $\langle 111 \rangle$ orientation of most grains after

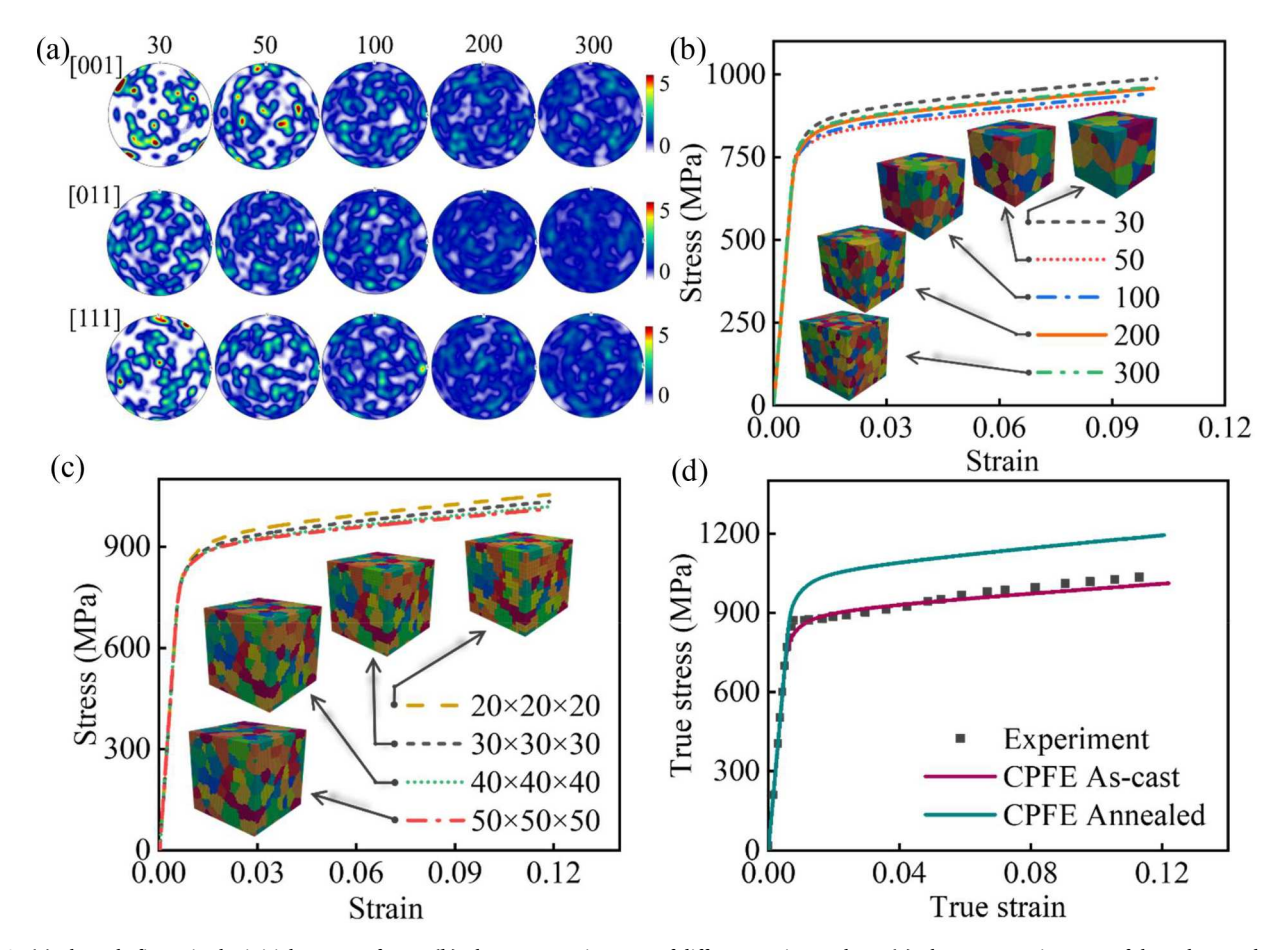


Fig. 16. (a) The pole figure in the initial texture of RVE. (b) The stress-strain curve of different grain numbers. (c) The stress-strain curve of the polycrystal with 200 grains for different element numbers. (d) Mechanical response of the as-cast and annealed HfNbTa from the simulated and experimental results.

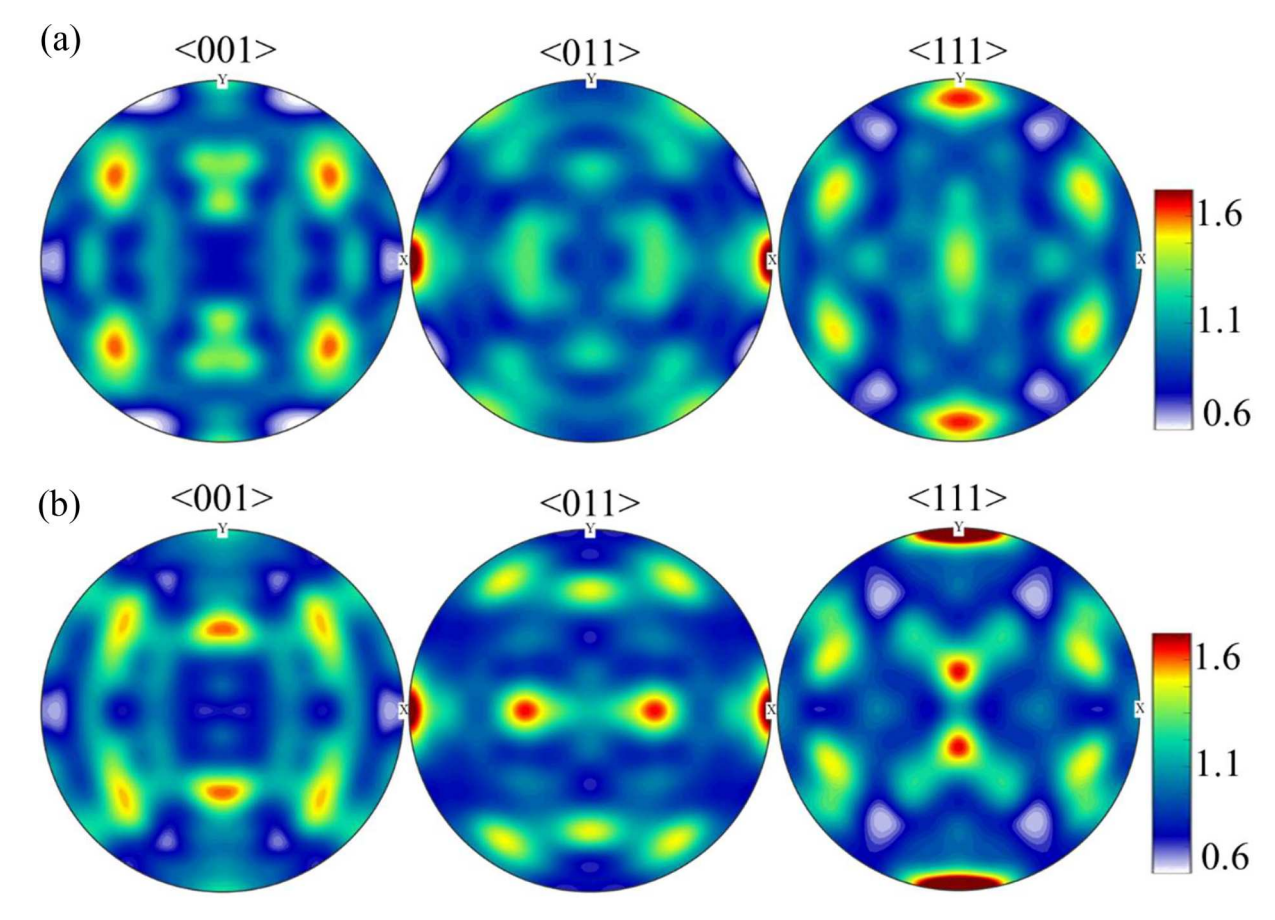


Fig. 17. The pole figure at the strain of 13 % in the (a) as-cast and (b) annealed HfNbTa.

rotation tends to the deformation axis, and finally a stable $\langle 111 \rangle$ texture is formed [82]. From Fig. 17, it can also be seen that the grain orientation is obviously different in the as-cast and annealed RMPEA. The positions of the maximum intensity move around between pole figures of the as-cast and annealed RMPEAs. Although the degree of the grain internal deformation is different, the relative uniform distribution occurs in the grain orientation. The annealed HfNbTa shows the stronger texture (Fig. 17), due to the local ordered structure refuses to permit the

free deformation of the materials at the high heterogeneous lattice strain [32].

Fig. 18 shows the spatial distribution of the von Mises equivalent strain after the loading to the strain of 0.5 %, 1 %, 5 %, and 12 %. To probe the deformation characteristics of each grain, the white lines showing the grain boundaries are overlaid on the strain maps. In generally, the model of the equivalent strain distribution is largely similar at each strain level from the yield point to strain hardening stage.

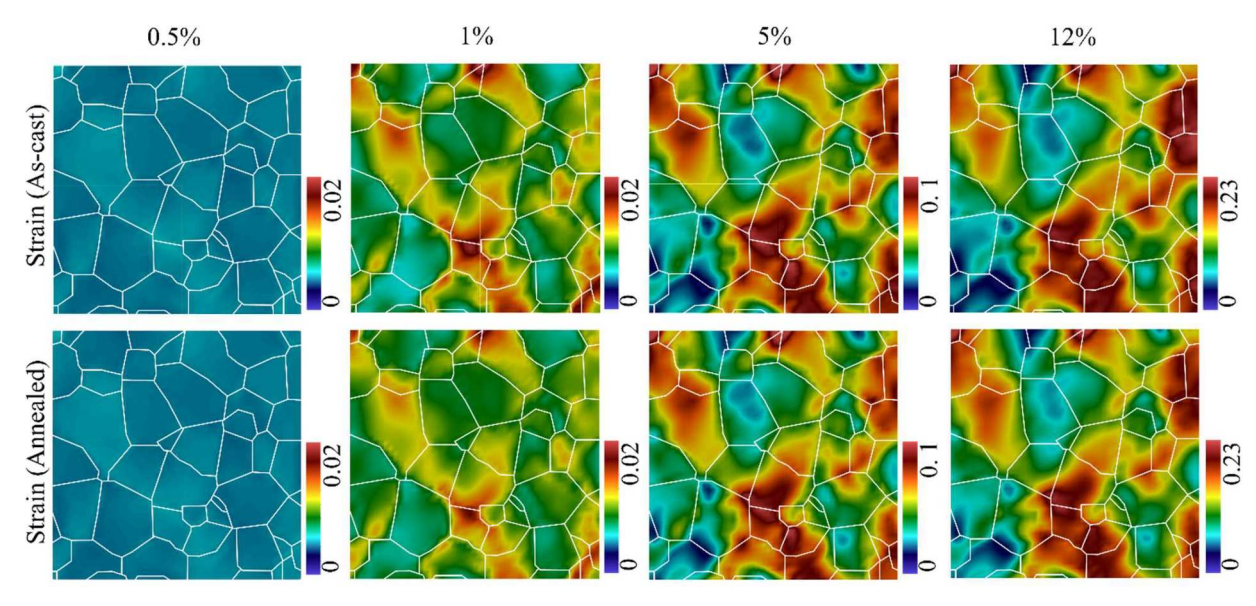


Fig. 18. Strain distribution of the as-cast and annealed HfNbTa RMPEA at the strain of 0.5 % (elastic stage), 1 % (yield point), 5 % and 12 % (plastic stage).

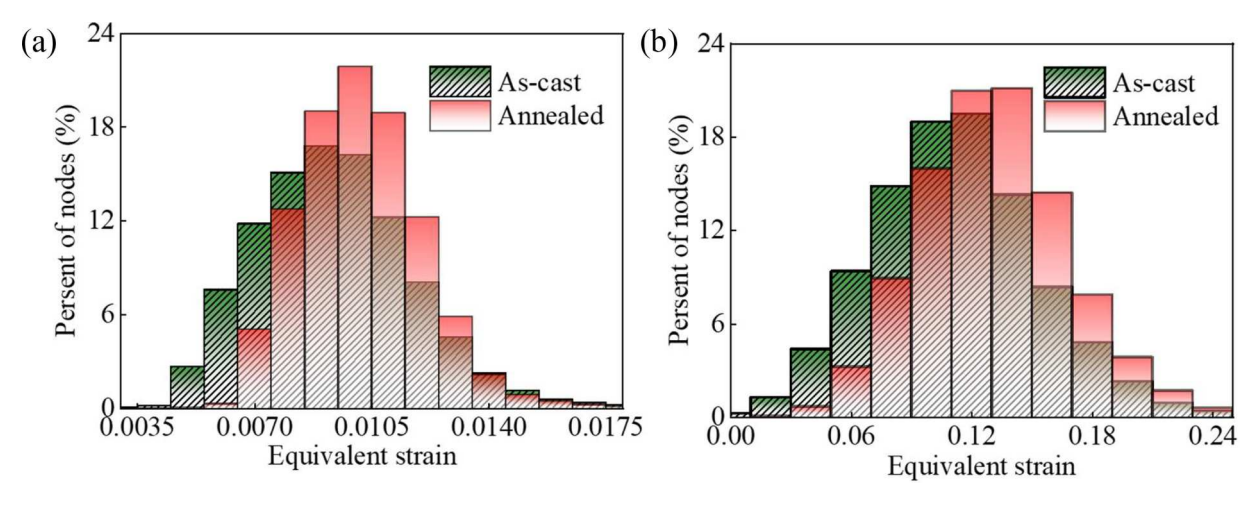


Fig. 19. Strain statistics of the as-cast and annealed HfNbTa RMPEA at the strain of (a) 1 % (yield point), and (b) 12 % (plastic stage).

As a result, the highly heterogeneous large equivalent strain is centrally distributed in several grains (Fig. 18), to adapt to the plastic deformation. Regardless of the HfNbTa RMPEA in the elastic and plastic deformation stages, some regions always maintain the lowest relative equivalent strain, corresponding to the locations containing the large grains. It is worth noting that the higher equivalent strain occurs in the annealed sample compared to the as-cast sample (Fig. 18). The existence of CSRO structure would be expected to suppress the dislocation slip or stacking-fault glide for increasing the difficulty of the plastic deformation, and raises the strength of the annealed HfNbTa RMPEA. For the NiCr alloys with high SRO degree, the occurrence of the extensive deformation twins together with microbands delay the decrease of strain hardening rate to a certain extent [75]. In the high specific strength steel, SRO would facilitate the planar slip for the high strain hardening rate [83]. The strength-plasticity synergy is observed in the CoCrNi MPEA with the local ordered structure owing to a strong lattice distortion generated in the compositional undulation [84]. Hence, the CSRO results in the obvious heterogeneous strain partitioning (Figs. 18 and 19), which forms a strong strain gradient in the adjacent grain interiors to act in response to the plastic deformation of the HfNbTa RMPEA.

In addition to the strain distribution, the partitioning of local von Mises stress is another important criterion for characterizing the plastic deformation behavior in the metallic materials [24,85]. The von Mises stress distribution is presented in Fig. 20. The relative high stress distribution pattern of the initial yielding stage is similar with the continuously increasing strain (Fig. 19), where the areas being close to the high stress gradually increases the stress amplitude. This trend is almost consistent with the changeable rule of the strain map, but the high equivalent strain may not reflect regional high stress conditions (Figs. 18 and 20). In comparison with the strain maps, the stress distribution shows relatively uniform except for a few obvious local stress concentrations. The annealed HfNbTa RMPEA exhibits the higher von Mises stress at the same strain level due to the CSRO (Fig. 21). The average value of the stress distribution is greater with the increased strain, indicating that the inhomogeneous degree of the von Mises stress distribution become more serious at the high strain to respond well to the plastic deformation of the high-strength HfNbTa RMPEA. In addition, the heterogeneous stress partitioning can surely contribute to the stronger back-stress-induced strain hardening in the annealed HfNbTa RMPEA. Simultaneously, the resultant change of internal von Mises stress distribution activated by the local ordered structure produces the localized and inhomogeneous deformation in some adjacent grains [86].

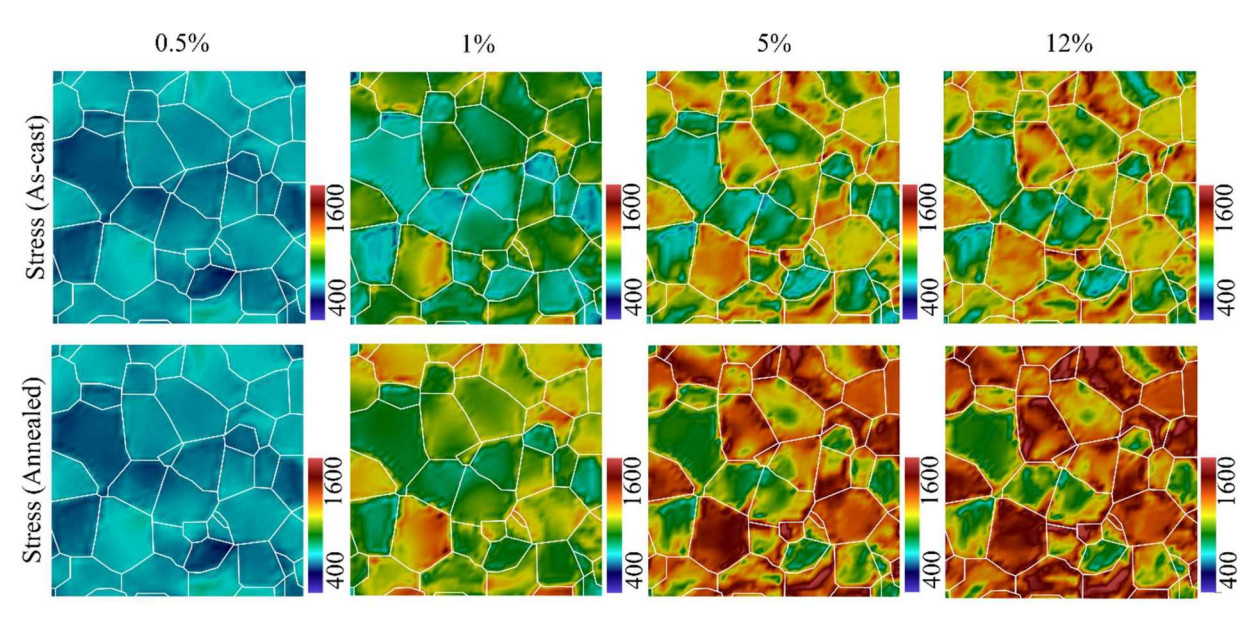


Fig. 20. Stress distribution of the as-cast and annealed HfNbTa at the strain of 0.5 % (elastic stage), 1 % (yield point), 5 %, and 12 % (plastic stage).

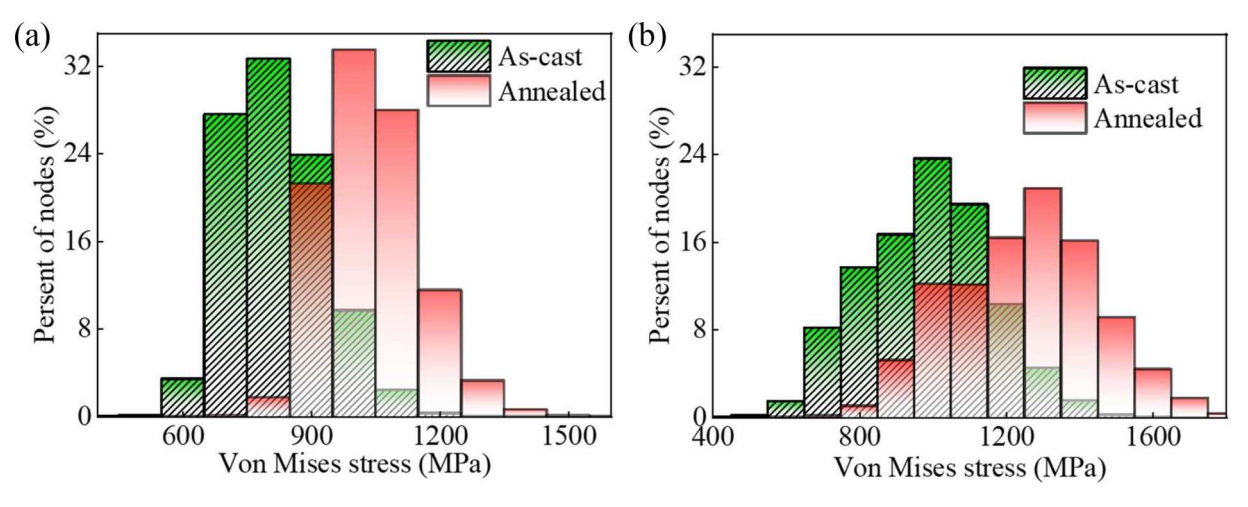


Fig. 21. Stress statistics of the as-cast and annealed HfNbTa at the strain of (a) 1 % (yield point), and (b) 12 % (plastic stage).

6. Conclusions

In the present work, we propose a crystal plastic method based on the hierarchical multiscale crystal plasticity model, to reveal the strengthening mechanism and deformation behavior in the BCC HfNbTa RMPEA. The current framework successfully captures the lattice strain fluctuations dominated by CSRO structure, and predicts the mechanical behavior of the as-cast and annealed HfNbTa under the tensile loading. The comparison of simulation and experiment shows that the developed framework accurately predicts the mechanical response of the HfNbTa at mesoscale. At the microscale, the local stress fluctuations caused by CSRO structure hinder dislocation slip, resulting in a significant increase in the strength of dislocation junctions for the forest networks. The mechanical behavior of the single crystal shows the annealed HfNbTa has higher strain hardening level than the as-cast sample. The CPFE simulations show that the annealed polycrystalline HfNbTa has stronger texture and more serious degree of inhomogeneous stress distribution at the high strain. The free deformation of the material is not allowed under high heterogeneous lattice strain, and local ordered structure refuses to permits free deformation under high heterogeneous lattice strain, to respond well to the plastic deformation of the high-strength HfNbTa. In addition, the plastic deformation in the annealed HfNbTa is difficult owing to the inhibition of dislocation slip. The CSRO leads to an obvious heterogeneous strain and stress partitioning, which forms a strong strain gradient in the adjacent grain interiors, and then contributes to the strong back-stress-induced strain hardening in the annealed HfNbTa. The multiscale crystal plasticity framework is very useful for optimizing and designing the composition heterogeneity of BCC multicomponent alloys to achieve both strength and toughness improvement.

CRediT authorship contribution statement

Weizheng Lu: Formal analysis, Software, Methodology, Investigation, Visualization, Validation, Data curation, Writing – original draft. Yang Chen: Formal analysis, Software, Methodology, Writing – original draft, Data curation. Wei Zhang: Investigation, Visualization, Methodology. Fusheng Tan: Investigation, Visualization, Methodology. Jia Li: Project administration, Methodology, Investigation, Visualization, Conceptualization, Writing – original draft. Bin Liu: Investigation, Visualization, Methodology, Validation. Peter K Liaw: Investigation, Visualization, Methodology, Writing – original draft. Qihong Fang: Project administration, Methodology, Investigation, Visualization, Conceptualization, Writing – original draft.

Declaration of competing interest

The authors declare that they have no known competing financial interests or personal relationships that could have appeared to influence the work reported in this paper.

Data availability

Data will be made available on request.

Acknowledgements

The authors would like to deeply appreciate the supports from National Natural Science Foundation of China (12372069, 12302083, U2267252, and 12172123), China Postdoctoral Science Foundation (2023M731061), Natural Science Foundation of Hunan Province (2022JJ20001), and the Hunan Provincial Innovation Foundation for Postgraduate (CX20220378). PKL very much appreciates the support from the National Science Foundation (DMR-1611180, 1809640, and 2226508).

References

- Li Z, Pradeep KG, Deng Y, Raabe D, Tasan CC. Metastable high-entropy dual-phase alloys overcome the strength-ductility trade-off. Nature 2016;534(7606):227–30.
- [2] Lei Z, Liu X, Wu Y, Wang H, Jiang S, Wang S, Hui X, Wu Y, Gault B, Kontis P. Enhanced strength and ductility in a high-entropy alloy via ordered oxygen complexes. Nature 2018;563(7732):546–50.
- [3] Ding Q, Zhang Y, Chen X, Fu X, Chen D, Chen S, Gu L, Wei F, Bei H, Gao Y. Tuning element distribution, structure and properties by composition in high-entropy allovs. Nature 2019;574(7777):223–7.
- [4] Feng R, Rao Y, Liu C, Xie X, Yu D, Chen Y, Ghazisaeidi M, Ungar T, Wang H, An K. Enhancing fatigue life by ductile-transformable multicomponent B2 precipitates in a high-entropy alloy. Nat Commun 2021;12(1):1–10.
- [5] Nene SS, Frank M, Liu K, Sinha S, Mishra RS, McWilliams BA, Cho KC. Corrosion-resistant high entropy alloy with high strength and ductility. Scr Mater 2019;166: 168–72.
- [6] Zhao S, Li Z, Zhu C, Yang W, Zhang Z, Armstrong DEJ, Grant PS, Ritchie RO, Meyers MA. Amorphization in extreme deformation of the CrMnFeCoNi highentropy alloy. Sci Adv 2021;7(5):eabb3108.
- [7] Frey C, Silverstein R, Pollock TM. A high stability B2-containing refractory multiprincipal element alloy. Acta Mater 2022;229:117767.
- [8] Cao PP, Huang HL, Jiang SH, Liu XJ, Wang H, Wu Y, Lu ZP. Microstructural stability and aging behavior of refractory high entropy alloys at intermediate temperatures. J Mater Sci Technol 2022;122:243–54.
- [9] Chen X, Wang Q, Cheng Z, Zhu M, Zhou H, Jiang P, Zhou L, Xue Q, Yuan F, Zhu J. Direct observation of chemical short-range order in a medium-entropy alloy. Nature 2021;592(7856):712–6.
- [10] Jian WR, Xie Z, Xu S, Su Y, Yao X, Beyerlein IJ. Effects of lattice distortion and chemical short-range order on the mechanisms of deformation in medium entropy alloy CoCrNi. Acta Mater 2020;199:352–69.

- [11] Zhang R, Zhao S, Ding J, Chong Y, Jia T, Ophus C, Asta M, Ritchie RO, Minor AM. Short-range order and its impact on the CrCoNi medium-entropy alloy. Nature 2020;581(7808):283–7.
- [12] Yin S, Ding J, Asta M, Ritchie RO. Ab initio modeling of the energy landscape for screw dislocations in body-centered cubic high-entropy alloys. Npj Comput Mater 2020;6(1):1–11.
- [13] Li QJ, Sheng H, Ma E. Strengthening in multi-principal element alloys with local-chemical-order roughened dislocation pathways. Nat Commun 2019;10(1):1–11.
- [14] Cao PY, Wang J, Jiang P, Wang YJ, Yuan FP, Wu XL. Prediction of chemical short-range order in high-/medium-entropy alloys. J Mater Sci Technol 2024;169: 115–23.
- [15] Wu Y, Zhang F, Yuan X, Huang H, Wen X, Wang Y, Zhang M, Wu H, Liu X, Wang H, Jiang S, Lu Z. Short-range ordering and its effects on mechanical properties of highentropy alloys. Mater Sci Technol 2021;62:214–20.
- [16] Ye YX, Lu ZP, Nieh TG. Dislocation nucleation during nanoindentation in a bodycentered cubic TiZrHfNb high-entropy alloy. Scr Mater 2017;130:64–8.
- [17] Yin S, Zuo Y, Abu-Odeh A, Zheng H, Li XG, Ding J, Ong SP, Asta M, Ritchie RO. Atomistic simulations of dislocation mobility in refractory high-entropy alloys and the effect of chemical short-range order. Nat Commun 2021;12(1):1–14.
- [18] Khoei AR, Jahanshahi M. Multi-scale modeling of plastic deformations in nanoscale materials; transition to plastic limit. Int J Numer Meth Eng 2017;109(8): 1180-216.
- [19] Yu S, Yang S, Cho M. Multiscale modeling of cross-linked epoxy nanocomposites to characterize the effect of particle size on thermal conductivity. J Appl Phys 2011; 110(12):124302.
- [20] Keshavarz S, Ghosh S, Reid ACE, Langer SA. A non-Schmid crystal plasticity finite element approach to multi-scale modeling of nickel-based superalloys. Acta Mater 2016;114:106–15.
- [21] Khoei AR, Ghahremani P. Temperature-dependent multi-scale modeling of surface effects on nano-materials. Mech Mater 2012;46:94–112.
- [22] Khoei AR, Sameti AR, Kazerooni YN. A continuum-atomistic multi-scale technique for nonlinear behavior of nano-materials. Int J Mech Sci 2018;148:191–208.
- [23] Jahanshahi M, Ahmadi H, Khoei AR. A hierarchical hyperelastic-based approach for multi-scale analysis of defective nano-materials. Mech Mater 2020;140:103206.
- [24] Fang Q, Lu W, Chen Y, Feng H, Liaw PK, Li J. Hierarchical multiscale crystal plasticity framework for plasticity and strain hardening of multi-principal element alloys. J Mech Phys Solids 2022:10s5067.
- [25] Eleti RR, Stepanov N, Yurchenko N, Klimenko D, Zherebtsov S. Plastic deformation of solid-solution strengthened Hf-Nb-Ta-Ti-Zr body-centered cubic medium/highentropy alloys. Scr Mater 2021;200:113927.
- [26] Yaghoobi M, Ganesan S, Sundar S, Lakshmanan A, Rudraraju S, Allison JE, Sundararaghavan V. PRISMS-plasticity: an open-source crystal plasticity finite element software. Comput Mater Sci 2019;169:109078.
- [27] Asaro RJ, Rice JR. Strain localization in ductile single crystals. J Mech Phys Solids 1977;25(5):309–38.
- [28] McDowell DL. Stress state dependence of cyclic ratchetting behavior of two rail steels. Int J Plast 1995;11:397–421.
- [29] Kalidindi SR, Bronkhorst CA, Anand L. Crystallographic texture evolution in bulk deformation processing of FCC metals. J Mech Phys Solids 1992;40(3):537–69.
- [30] Stopka KS, Yaghoobi M, Allison JE, McDowell DL. Simulated effects of sample size and grain neighborhood on the modeling of extreme value fatigue response. Acta Mater 2022;224:117524.
- [31] Hao S, Liu WK, Moran B, Vernerey F, Olson GB. Multi-scale constitutive model and computational framework for the design of ultra-high strength, high toughness steels. Comput Methods Appl Mech Eng 2004;193(17–20):1865–908.
- [32] Li J, Chen Y, He Q, Xu X, Wang H, Jiang C, Liu B, Fang Q, Liu Y, Yang Y. Heterogeneous lattice strain strengthening in severely distorted crystalline solids. Proc Natl Acad Sci U S A 2022;119(25):e2200607119.
- [33] Zeng Z, Li X, Xu D, Lu L, Gao H, Zhu T. Gradient plasticity in gradient nano-grained metals. Extreme Mech Lett 2016;8:213–9.
- [34] Khoei AR, Kianezhad M. A machine learning-based atomistic-continuum multiscale technique for modeling the mechanical behavior of Ni3Al. Int J Mech Sci 2022: 107858
- [35] Chakraborty S, Ghosh S. A concurrent atomistic-crystal plasticity multiscale model for crack propagation in crystalline metallic materials. Comput Methods Appl Mech Eng 2021;379:113748.
- [36] Chaussidon J, Fivel M, Rodney D. The glide of screw dislocations in bcc Fe: atomistic static and dynamic simulations. Acta Mater 2006;54(13):3407–16.
- [37] Plimpton S. Fast parallel algorithms for short-range molecular dynamics. J Comput Phys 1995;117(1):1–19.
- [38] Stukowski A. Visualization and analysis of atomistic simulation data with OVITO-the open visualization tool. Modell Simul Mater Sci Eng 2009;18(1): 015012.
- [39] Gilbert MR, Queyreau S, Marian J. Stress and temperature dependence of screw dislocation mobility in α-Fe by molecular dynamics. Phys Rev B 2011;84(17): 174102
- [40] Xu S, Jian WR, Su Y, Beyerlein IJ. Line-length-dependent dislocation glide in refractory multi-principal element alloys. Appl Phys Lett 2022;120(6):061901.
- [41] Sills RB, Foster ME, Zhou XW. Line-length-dependent dislocation mobilities in an FCC stainless steel alloy. Int J Plast 2020;135:102791.
- [42] Huang X, Liu L, Duan X, Liao W, Huang J, Sun H, Yu C. Atomistic simulation of chemical short-range order in HfNbTaZr high entropy alloy based on a newlydeveloped interatomic potential. Mater Des 2021;202:109560.
- [43] Chen S, Aitken ZH, Pattamatta S, Wu Z, Yu ZG, Srolovitz DJ, Liaw PK, Zhang YW. Simultaneously enhancing the ultimate strength and ductility of high-entropy alloys via short-range ordering. Nat Commun 2021;12(1):4953.

- [44] Li QJ, Sheng H, Ma E. Strengthening in multi-principal element alloys with local-chemical-order roughened dislocation pathways. Nat Commun 2019;10:3563.
- [45] Maiti S, Steurer W. Structural-disorder and its effect on mechanical properties in single-phase TaNbHfZr high-entropy alloy. Acta Mater 2016;106:87–97.
- [46] Huang YC, Lai YC, Lin YH, Wu SK. A study on the severely cold-rolled and annealed quaternary equiatomic derivatives from quinary HfNbTaTiZr refractory high entropy alloy. J Alloys Compd 2021;855:157404.
- [47] He Q, Yoshida S, Yasuda H, Tsuji N. Effect of elemental combination on microstructure and mechanical properties of quaternary refractory medium entropy alloys. Mater Trans 2020;61(4):577–86.
- [48] Chen Y, Feng H, Li J, Liu B, Jiang C, Liu Y, Fang QH, Liaw PK. Dislocation flow turbulence simultaneously enhances strength and ductility. Proc Natl Acad Sci U S A 2024
- [49] Bulatov V, Cai W. Computer simulations of dislocations. Oxford University Press; 2006
- [50] Arsenlis A, Rhee M, Hommes G, Cook R, Marian J. A dislocation dynamics study of the transition from homogeneous to heterogeneous deformation in irradiated bodycentered cubic iron. Acta Mater 2012;60(9):3748–57.
- [51] Voyiadjis GZ, Abed FH. Microstructural based models for bcc and fcc metals with temperature and strain rate dependency. Mech Mater 2005;37(2–3):355–78.
- [52] Cui Y, Po G, Ghoniem N. Temperature insensitivity of the flow stress in bodycentered cubic micropillar crystals. Acta Mater 2016;108:128–37.
- [53] Chandra S, Samal MK, Chavan VM, Raghunathan S. Hierarchical multiscale modeling of plasticity in copper: from single crystals to polycrystalline aggregates. Int J Plast 2018;101:188–212.
- [54] Fan H, Wang Q, El-Awady JA, Raabe D, Zaiser M. Strain rate dependency of dislocation plasticity. Nat Commun 2021;12(1):1–11.
- [55] Po G, Cui Y, Rivera D, Cereceda D, Swinburne TD, Marian J, Ghoniem NJAM. A phenomenological dislocation mobility law for bcc metals. Acta Mater 2016;119: 123–25
- [56] Bangerth W, Hartmann R, Kanschat G. deal. II—A general-purpose object-oriented finite element library. ACM Trans Math Softw 2007;33(4):24–es.
- [57] Groeber MA, Jackson MA. DREAM. 3D: a digital representation environment for the analysis of microstructure in 3D. Integr Mater Manuf I 2014;3(1):56–72.
- [58] J. Ahrens, B. Geveci, C. Law, Paraview: an end-user tool for large data visualization, the visualization handbook 717(8) (2005).
- [59] Yalcinkaya T, Brekelmans WAM, Geers MGD. BCC single crystal plasticity modeling and its experimental identification. Modell Simul Mater Sci Eng 2008;16 (8):085007.
- [60] Groh S, Marin EB, Horstemeyer MF, Zbib HM. Multiscale modeling of the plasticity in an aluminum single crystal. Int J Plast 2009;25(8):1456–73.
- [61] Li Q, Zhang H, Chen F, Xu D, Sui D, Cui Z. Study on the plastic anisotropy of advanced high strength steel sheet: experiments and microstructure-based crystal plasticity modeling. Int J Mech Sci 2020;176:105569.
- [62] Cai W, Song Q, Ji H, Liu Z. Dual-phase morphology distribution effects on mechanical behaviors of Ti6Al4V via pseudorandom crystal plasticity modeling. J Mater Res Technol 2022;17:2897–912.
- [63] Kim JH, Lee MG, Kang JH, Oh CS, Barlat F. Crystal plasticity finite element analysis of ferritic stainless steel for sheet formability prediction. Int J Plast 2017;93:26–45.
 [64] Esfandiarpour A, Papanikolaou S, Alava M, Edge dislocations in multicomponent
- [64] Esfandiarpour A, Papanikolaou S, Alava M. Edge dislocations in multicomponent solid solution alloys: beyond traditional elastic depinning. Phys Rev Res 2022;4(2): 1022043.
- [65] Chen B, Li S, Zong H, Ding X, Sun J, Ma E. Unusual activated processes controlling dislocation motion in body-centered-cubic high-entropy alloys. Proc Natl Acad Sci U S A 2020;117(28):16199–206.
- [66] Ye YF, Zhang YH, He QF, Zhuang Y, Wang S, Shi SQ, Hu A, Fan J, Yang Y. Atomic-scale distorted lattice in chemically disordered equimolar complex alloys. Acta Mater. 2018;150:182–94
- [67] Rida A, Martinez E, Rodney D, Geslin PA. Influence of stress correlations on dislocation glide in random alloys. Phys Rev Mater 2022;6(3):033605.
- [68] Kulesza S, Bramowicz M. A comparative study of correlation methods for determination of fractal parameters in surface characterization. Appl Surf Sci 2014; 293:196–201.
- [69] Ausloos M, Berman DH. A multivariate Weierstrass-Mandelbrot function. Proc R Soc Ser A 1985;400(1819):331–50.
- [70] Wu JJ. Analyses and simulation of anisotropic fractal surfaces. Chaos Solitons Fractals 2002;13(9):1791–806.
- [71] Zhang HT, Fu HD, He XQ, Wang CS, Jiang L, Chen LQ, Xie JX. Dramatically enhanced combination of ultimate tensile strength and electric conductivity of alloys via machine learning screening. Acta Mater 2020;200:803–10.
- [72] Zhou X, He S, Marian J. Cross-kinks control screw dislocation strength in equiatomic bcc refractory alloys. Acta Mater 2021;211:116875.
- [73] Bu Y, Wu Y, Lei Z, Yuan X, Wu H, Feng X, Liu J, Ding J, Lu Y, Wang H. Local chemical fluctuation mediated ductility in body-centered-cubic high-entropy alloys. Mater Today 2021;46:28–34.
- [74] Wang X, Maresca F, Cao P. The hierarchical energy landscape of screw dislocation motion in refractory high-entropy alloys. Acta Mater 2022;234:118022.
- [75] Wang F, Balbus GH, Xu S, Su Y, Shin J, Rottmann PF, Knipling KE, Stinville JC, Mills LH, Senkov ON. Multiplicity of dislocation pathways in a refractory multiprincipal element alloy. Science 2020;370(6512):95–101 (1979).
- [76] Laplanche G, Bonneville J, Varvenne C, Curtin WA, George EP. Thermal activation parameters of plastic flow reveal deformation mechanisms in the CrMnFeCoNi high-entropy alloy. Acta Mater 2018;143:257–64.
- [77] Zhang P, Shi K, Bian J, Zhang J, Peng Y, Liu G, Deschamps A, Sun J. Solute cluster evolution during deformation and high strain hardening capability in naturally aged Al–Zn–Mg alloy. Acta Mater 2021;207:116682.

- [78] Madec R, Kubin LP. Second-order junctions and strain hardening in bcc and fcc crystals. Scr Mater 2008;58(9):767–70.
- [79] Li L, Fang Q, Li J, Liu B, Liu Y, Liaw PK. Lattice-distortion dependent yield strength in high entropy alloys. Mater Sci Eng A 2020;784:139323.
- [80] Fan XJ, Qu RT, Zhang ZF. Remarkably high fracture toughness of HfNbTaTiZr refractory high-entropy alloy. J Mater Sci Technol 2022;123:70–7.
- [81] Xiong W, Guo A, Zhan S, Liu C, Cao S. Remarkably high fracture toughness of HfNbTaTiZr refractory high-entropy alloy. J Mater Sci Technol 2023;142:196–215.
- [82] Eleti RR, Chokshi AH, Shibata A, Tsuji N. Unique high-temperature deformation dominated by grain boundary sliding in heterogeneous necklace structure formed by dynamic recrystallization in HfNbTaTiZr BCC refractory high entropy alloy. Acta Mater 2020;183:64–77.
- [83] Kim H. Strain hardening of novel high Al low-density steel consisting of austenite matrix and B2-ordered intermetallic second phase in the perspective of non-cell forming face-centered-cubic alloy with high stacking fault energy. Scr Mater 2019; 160:29–32.
- [84] Zhu J, Sun L, Li D, Zhu L, He X. Compositional undulation induced strain hardening and delocalization in multi-principal element alloys. Int J Mech Sci 2022:107931.
- [85] Tasan CC, Diehl M, Yan D, Zambaldi C, Shanthraj P, Roters F, Raabe D. Integrated experimental–simulation analysis of stress and strain partitioning in multiphase alloys. Acta Mater 2014;81:386–400.
- [86] Tsianikas S, Chen Y, Slattery A, Peters J, Xie Z. Adaptive attenuation of hierarchical composition fluctuations augments the plastic strain of a high entropy steel. Mater Sci Eng A 2022;857:144037.